J. Fluid Mech. (1992), *vol.* 235, *pp.* 1–36
Printed in Great Britain

Buoyancy- and thermocapillary-driven flows in differentially heated cavities for low-Prandtl-number fluids

By HAMDA BEN HADID[1] AND BERNARD ROUX[2]

[1] Laboratoire de Mécanique des Fluides & d'Acoustique, URA 263, Ecole Centrale de Lyon, BP 163, 69131 Ecully Cedex, France

[2] Institut de Mécanique de Marseille, UM 34, 1, rue Honnorat 13003, Marseille, France

(Received 7 March 1990 and in revised form 12 July 1991)

The influence of thermocapillary forces on buoyancy-driven convection is numerically simulated for shallow open cavities with differentially heated endwalls and filled with low-Prandtl-number fluid. Calculations are carried out by solving two-dimensional Navier–Stokes equations coupled to the energy equation, for three aspects ratios A = (length/height) = 4, 12.5 and 25, and several values of the Grashof number (up to 6×10^4) and Reynolds number ($|Re| \leqslant 1.67 \times 10^4$). Thermocapillarity can have a quite significant effect on the stability of a primarily buoyancy-driven flow. The result of the combination of the two basic mechanisms (thermocapillarity) and buoyancy) depends on whether their effects are additive (positive Re) or opposing (negative Re); counter-acting mechanisms yield more complex flow patterns. The critical Grashof number Gr_c for the onset of the unsteady regime is found to decrease substantially within a small range of negative Re, and to increase for positive Re (and also for large negative Re). For $Gr = 4 \times 10^4$, $A = 4$ and small negative Reynolds numbers, $-2.4 \times 10^3 \leqslant Re < 0$, mono-periodic and bi- or quasi-periodic regimes are shown to exist successively, followed by a reverse transition. The development of the instabilities from an initial steady-state regime has been investigated by varying Re for $Gr = 1.5 \times 10^4$ (below Gr_c at $Re = 0$); the onset of buoyant instabilities is enhanced in a narrow range of Re only ($-1200 < Re < -200$). It is also noteworthy that for small enough Grashof numbers (e.g. $Gr = 3 \times 10^3$), a steady-state solution prevails over the whole range of Reynolds numbers investigated. This means that a critical Grashof number exists below which the effect of the thermocapillary forces is no longer destabilizing.

1. Introduction

The present study addresses combined buoyancy and thermocapillary convection in fluid contained in shallow open cavities, where the flow is driven by a temperature difference between isothermal vertical sidewalls. In this system with a free liquid–gas interface, the imposed temperature gradient generates simultaneously buoyancy-driven convection (due to a density variation in the liquid) and thermocapillary-driven convection (due to a surface-tension gradient induced by a temperature gradient along the liquid–gas interface). Attention is focused on the interaction of these two types of convections, which can coexist in a 1−g as well as a low-gravity environment (Carruthers 1977*a*; Ostrach & Pradhan 1978; Schwabe 1988; Schwabe & Scharmann 1981; Ostrach 1982; Gershuni, Zhukhovitsky & Nepomniashchy

1989). Our interest in such flows arises from their importance for many engineering systems such as that of crystal growth where the quality of the crystal grown can be strongly influenced by the fluid motion. More precisely this numerical study was motivated by experiments conducted by Favier and co-workers to gain a fundamental understanding of thermocapillary effect on growing metallic single crystals (e.g. see Camel, Tison & Favier 1986; Camel & Favier 1988). So, up to now results have been restricted to low-Prandtl-number fluids (typically, $Pr = 0.015$). Reviews of the work concerning hydrodynamic aspects of crystal growth can be found in the survey papers of Carruthers (1977*b*), Pimputkar & Ostrach (1981), Azouni (1981), Hurle (1983), Polezhaev (1984), Langlois (1985) and Müller (1988) for example. Note that despite the technological importance of low-Prandtl-number fluids there is a lack of experimental velocity and temperature field measurements as they are very difficult to obtain owing to opacity, temperature level, etc.

Experimental investigations (Utech, Brower & Early 1967; Hurle, Jakeman & Johnson 1974; Chun 1980; Favier, Rouzaud & Comera 1986, among others) have shown that temperature fluctuations, caused by an unsteady buoyancy-driven convective flow, occur when the thermal gradient exceeds a certain critical value. These instabilities are known to contribute to the inhomogeneity of the resulting crystal (Hurle 1967; Carruthers 1977*b*; Rosenberger 1979; Polezhaev 1984; and Müller 1988). However, the basic mechanisms giving rise to these instabilities are still not well understood owing to their complexity.

Our main goal is to clarify the laminar flow transitions from a steady state to an oscillatory state, a problem which received special attention in the case of purely buoyancy-driven flow during a recent GAMM-Workshop (Roux 1990). As most of the growing techniques involve containers with small width (relative to the vertical plane defined by the gravity force and the imposed temperature gradient), the present numerical study is restricted to as two-dimensional model in a rectangular cavity of aspect ratio A, where A = length/depth. The relevant dimensionless parameters are the Prandtl, Grashof and surface-tension Reynolds numbers, which are defined as $Pr = \nu/\kappa$, $Gr = g\beta H^4 \Delta T/L\nu^2$ and $Re = (-\partial\sigma/\partial T) H^2 \Delta T/L\rho\nu^2$. Sometimes, the classical Marangoni number, $Ma = Re\,Pr$, will be also used. The relative magnitude of buoyancy to thermocapillary forces is given by the dynamical bond number, defined as $Bd = Gr/Re = \rho g\beta H^2/(-\partial\sigma/\partial T)$.

We will first consider a cavity with a moderate aspect ratio, $A = 4$, and various Grashof number values up to $Gr = 4 \times 10^4$, which is larger than the critical value for the transition to an unsteady flow (see §2.1). Both negative and positive values of Reynolds number (corresponding to positive and negative values of $\partial\sigma/\partial T$, respectively) will be considered. In fact, most real fluids have negative $\partial\sigma/\partial T$, but for certain alloys under certain conditions $\partial\sigma/\partial T$ can be positive (e.g. tin–bismuth with 5% bismuth, studied by Camel & Favier 1988). We will also study the flow regimes in larger cavities with $A = 12.5$ and 25, for two values of Grashof number, $Gr = 3 \times 10^3$ and 6×10^3 which are below the critical one for an infinitely long cavity (see §2.1). A specific study of steady-state regimes will be presented in §6 giving correlation laws characterizing the surface velocity for large-aspect-ratio cavities, $4 \leqslant A \leqslant 25$, at large enough $|Re|$.

This paper complements a previous one by Ben Hadid, Laure & Roux (1989) on the same topic, but devoted to the case of $A = 25$ and containing theoretical results.

2. Summary of previous work

2.1. *Oscillations in purely buoyancy-driven flows*

By means of a stability analysis of the one-dimensional solution given by Birikh (1966) for flows in an infinite horizontal fluid layer with a free surface ($Re = 0$), Laure & Roux (1987) showed that the first bifurcation to an unsteady flow regime corresponds to a two-dimensional structure; the critical Grashof number for $Pr \to 0$ is $Gr_c = 7890$. For $Pr = 0.015$, they found $Gr_c = 1.064 \times 10^4$ for the case of a conducting wall and $Gr_c = 1.6 \times 10^4$ for an insulating wall.

For rectangular cavities of finite aspect ratio, Winters, Cliffe & Jackson (1987), and Winters (1988, 1990) carried out two-dimensional calculations and used bifurcation theory, and also determined the critical Grashof number for the transition from steady to unsteady flow. For $Pr = 0$ and $A = 4$, they found $Gr_c \approx 1.37 \times 10^4$ which is about 75% higher than for infinite layer ($A \to \infty$). They showed that Gr_c decreases with increasing aspect ratio and thus qualitatively confirmed the experimental results of Hurle *et al.* (1974). (See Roux, Ben Hadid & Laure 1989.) In addition, Winters (1990) pointed out a dependence of Gr_c on the horizontal thermal boundary conditions, e.g. for $Pr = 0.015$, $Gr_c \approx 1.66 \times 10^4$ in the insulating case, and $Gr_c \approx 1.48 \times 10^4$ in the conducting case. Thus, Gr_c is higher in the insulating case; in fact, the difference between it and the conducting case becomes larger and larger as Pr increases. This effect of horizontal thermal boundary conditions was numerically confirmed by Ben Hadid (1989) and Pulicani (1989). The increase in stability for the insulating case is probably due to the temperature stratification, which is more effective in this case than for the conducting case.

Numerical results by Ben Hadid & Roux (1990*a*) and by Randriamampianina *et al.* (1990) also showed that the two-dimensional oscillatory regimes are maintained for $Gr \gg Gr_c$, in contrast with the case of a cavity with a rigid top (see the synthesis of the GAMM-Workshop, Roux 1990). The accurate spectral method used by Randriamampianina *et al.* (1990) indicates that the oscillatory regime is mono-periodic until $Gr \approx 2 \times 10^5$ (which is 15 times higher than Gr_c) and then a period doubling occurs.

2.2. *Pure thermocapillary flow*

The general class of flows induced by a thermocapillary force has been the subject of review articles by Levich & Krilov (1969), Ostrach (1982) and Davis (1987). There are a number of analytical papers about thermocapillary flows in a horizontal layer (see, for example, Birikh 1966; Yih 1968). Smith & Davis (1983) and Davis (1987) performed stability analyses of thermocapillary-driven flows subject to three-dimensional disturbances.

Numerical calculations of thermocapillary-driven flows in open cavities were performed by Strani, Piva & Graziani (1983) for moderate aspect ratios ($A \leqslant 5$), and by Wilke & Löser (1983) and Ben Hadid & Roux (1990*b*) for large aspect ratios ($A = 4$, 12.5 and 25). Ben Hadid *et al.* (1988) gave numerical results for the surface velocity in shallow cavities and showed that there is a transition from a viscous to a boundary-layer flow regime as the Reynolds number is increased, in agreement with experimental results of Camel *et al.* (1986). The limiting value of Re for the viscous regime was estimated to be $Re/A < 20$, while the transition to the boundary-layer regime occurs for $Re/A > 200$. For the boundary-layer regime, the surface velocity at the middle of the cavity (scaled by $\nu Re/H$) is given by a simple relationship: $v_{(x-1,\, y-A/2)} = 0.95\ (Re/A)^{-\frac{1}{2}}$.

Thermocapillary convection was observed under reduced gravity during the

Spacelab D1 mission (Metzger & Schwabe 1988; Lamprecht, Schwabe & Scharmann 1990). Metzger & Schwabe (1988) studied the effect of the aspect ratio for deep cavities ($A < 1$) by the varying the height of the cavity. They found that the surface velocity does not vary significantly when the aspect ratio is decreased. This indicates that the dynamical behaviour in deep and shallow cavities is fundamentally different.

In addition, a numerical study by Zebib, Homsy & Meiburg (1985) showed a substantial change in flow structure when Pr varies from 0.01 to 50. The centre of the strong vortex, and subsequently the maximum of the surface velocity, are located near the cold wall for low Prandtl numbers and near the hot wall for $Pr = 50$. This is the result of a larger interaction between fluid flow and thermal field for larger Pr.

2.3. *Combined buoyancy and thermocapillary forces*

Laure & Roux (1989) also performed a stability analysis of the Birikh (1966) solution for $A \to \infty$, in the case of a free surface with $Re \neq 0$. They found that the first bifurcation to an unsteady flow regime corresponds to a two-dimensional structure and occurs at a critical Grashof number, Gr_c, which tends asymptotically to a limiting value when $Pr \to 0$. This limit strongly depends on the ratio Re/Gr which characterizes the relative influence of thermocapillarity and buoyancy. Laure & Roux (1989) found, for example, $Gr_c \approx 1.6 \times 10^4$ for $Re/Gr = 0.025$. This is in agreement with the previous results by Myznikov (1981) for $W = 0.1$ (where $W = 4\,Re/Gr$) reported by Gershuni *et al.* (1989); these results were also reported by Polezhaev (1984) but unfortunately with an inconsistent definition of the parameters. All these results show that thermocapillarity delays the onset of buoyancy-induced oscillations, for positive Re. Critical values (neutral stability curves) of Gr_c have been also obtained for negative Re, at various Pr. For a fixed Pr, in the interval $10^{-3} \leqslant Pr \leqslant 5 \times 10^{-2}$, the stability diagram of Gr_c in terms of Re presents a minimum for $Re \approx -300$ (see figure 3 in Ben Hadid *et al.* 1989). It is interesting to note that the experiments of Camel *et al.* (1986) for liquid tin ($Pr \approx 0.015$) in large-aspect-ratio cavities did not exhibit time-dependent flow.

Kirdyashkin (1984) compared analytical results with experimental data for large horizontal cavities $7 \leqslant A \leqslant 90$ filled with larger-Prandtl-number liquids (water, ethyl-alcohol 96%), and showed that far from the endwalls the flow is plane-parallel. As a rule there is satisfactory agreement between experimental and analytical values in the case of a small temperature gradient.

Experimental results for combined buoyancy and thermocapillary flows in cavities have been performed by Villers & Platten (1987*a*) and Villers (1989) in a water–ethanol mixture ($Pr \approx 4$–7). In that case oscillatory regimes with a maximum of amplitude perturbation near the free surface were observed, indicating that the oscillations are induced at the surface. In addition, the authors showed that these oscillations are damped when the depth of liquid is increased and thus demonstrated the stabilizing effect of buoyancy forces in this case.

Ground-based experiments performed by Lamprecht *et al.* (1990) for paraffin ($Pr \approx 49$) in a small-aspect-ratio cavity ($A = 12$ and 0.5) revealed that for small values of the temperature difference ($\Delta T \approx 10°$, i.e. $Gr \approx 6 \times 10^4$ and $Re \approx 1.6 \times 10^3$) one large convection cell was formed, but when the temperature difference is increased ($\Delta T \approx 60°$) the flow structure separates into two distinct complicated parts (thermocapillary-driven near the free surface and buoyancy-driven in the rest of the cavity). These types of flow structures are more noticeable for lower aspect ratio (e.g. $A = 0.5$). This behaviour was also found by Metzger & Schwabe (1988) for ethanol

($Pr \approx 17$), a one-main-cell structure filling the cavity for $\Delta T \approx 1°$ ($Gr \approx 3.6 \times 10^4$ and $Re \approx 1 \times 10^3$), and a two-cell structure with an upper cell controlled by thermocapillarity and a lower cell controlled by buoyancy for $\Delta T \approx 4°$ ($Gr \approx 1.4 \times 10^5$ and $Re \approx 4 \times 10^3$). In addition, Metzger & Schwabe (1988) used a system with two sets of heating blocks allowing a temperature gradient to be generated in the bulk (positive or negative) independently from that along the free surface. They showed that even at high Grashof numbers (caused by increasing the cavity depth) the thermocapillarity is the dominant mechanism near the upper surface. Both positive and negative Grashof numbers enhance the velocity in the surface vortex.

Kamotani, Ostrach & Lowry (1982) also performed experiments for large-aspect-ratio cavities with radiative heating from a line source placed above the free surface of silicone oil or fluorinert fc-43. For the latter fluid the authors showed a weak temperature fluctuation near the free surface. Unfortunately they did not give any values for their dimensionless parameters. However, they mention that this oscillation is of small magnitude and its behaviour is not as well defined as in a half-floating-zone configuration (cylindrical geometry), for $Ma > 10^4$.

It is also interesting to mention that numerous experiments have been performed for full or half-floating-zone configurations and showed that combined buoyancy and thermocapillary convection can often lead to oscillatory regimes, sometimes with complex behaviour, e.g. oscillations with amplitude modulation (see, for example, the survey paper by Schwabe 1988).

Combined buoyancy and thermocapillary convection in a differentially heated cavity has also been the subject of several numerical studies. Cavities with $A = 1$ were considered by Zebib *et al.* (1985), Cuvelier & Driessen (1986) and Bradley & Homsy (1989). Bergman & Ramadhyani (1986) and Bergman & Keller (1988) presented computational results for $A \geqslant 1$. The effect of thermocapillary forces on the buoyancy-driven oscillatory flow in a cavity with $A = 4$, $Pr = 0.015$ and conducting horizontal boundaries was studied by Villers & Platten (1990) for $-20 \leqslant Ma \leqslant 200$ and $10^4 \leqslant Gr \leqslant 5 \times 10^4$, and by Ben Hadid & Roux (1989) for $-2 \times 10^3 \leqslant Re \leqslant 8 \times 10^2$ and $1.45 \times 10^4 \leqslant Gr \leqslant 2 \times 10^4$. These numerical results all show that a small negative Re (opposing effect) provides a destabilizing force and that when Re decreases the frequency and the mean flow rate decrease while the amplitude of the oscillations increases. On the other hand, if an oscillatory solution exists for a given Re and is taken as the initial state, these initial oscillations can be damped by increasing Re; in fact, the flow reaches its steady state more and more rapidly as Re increases.

3. Problem description

3.1. *Governing equations*

We consider a two-dimensional rectangular cavity of length L and height H as shown in figure 1. The vertical sidewalls of the cavity are maintained at temperatures T_h and T_c, where $T_h > T_c$. The surface tension on the upper boundary is assumed to vary linearly with temperature: $\sigma = \sigma_0[1-\gamma(T-T_0)]$ where $\gamma = -(1/\sigma_0)(\partial\sigma/\partial T)$ is the temperature coefficient of surface tension and where the subscript 0 refers to a reference state. The upper boundary is assumed to be flat ($Ca = |\partial\sigma/\partial T|\Delta T/\sigma_0 \ll 1$) and the fluid above the surface is assumed to be a gas of negligible viscosity and conductivity, and therefore, will not influence the flow and temperature fields in the liquid. The problem is non-dimensionalized by using H^2/ν, H, and $\Delta T/A$, as scale quantities for respectively time, length and temperature, where $\Delta T = T_h - T_c$ and ν

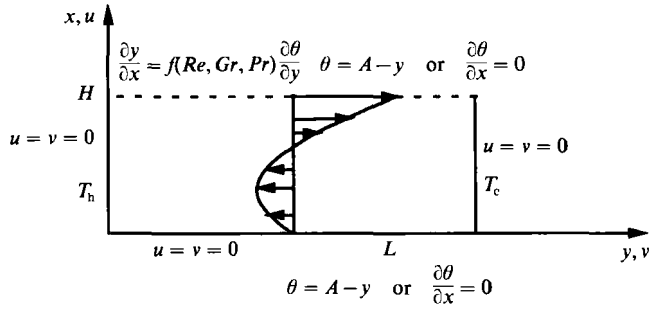

FIGURE 1. Geometry of the two-dimensional model. The sidewalls are differentially heated and the upper boundary is a flat free surface subject to thermocapillary effects.

is the kinematic viscosity. As our main interest is the influence of the thermocapillarity on an established buoyancy-driven flow, a characteristic buoyancy velocity, $\nu Gr^{\frac{1}{2}}/H$, is used as the reference velocity. The dimensionless equations governing the motion of a Newtonian fluid in the Boussinesq approximation may be written in a vorticity–stream function formulation as

$$\frac{\partial \zeta}{\partial t} + Gr^{\frac{1}{2}}\left[u\frac{\partial \zeta}{\partial x} + v\frac{\partial \zeta}{\partial y}\right] = \frac{\partial^2 \zeta}{\partial x^2} + \frac{\partial^2 \zeta}{\partial y^2} + Gr^{\frac{1}{2}}\frac{\partial \theta}{\partial y}; \tag{1}$$

$$\frac{\partial \psi}{\partial \tau} = \frac{\partial^2 \psi}{\partial x^2} + \frac{\partial^2 \psi}{\partial y^2} + \zeta; \tag{2}$$

$$\frac{\partial \theta}{\partial t} + Gr^{\frac{1}{2}}\left[u\frac{\partial \theta}{\partial x} + v\frac{\partial \theta}{\partial y}\right] = \frac{1}{Pr}\left[\frac{\partial^2 \theta}{\partial x^2} + \frac{\partial^2 \theta}{\partial y^2}\right]; \tag{3}$$

where ζ, ψ, and θ are the vorticity, the stream function and the temperature, respectively, and τ is a fictitious time introduced in (2) in order to accelerate the convergence procedure. The computational procedure was similar for each Grashof number: when a steady-state solution for large $|Re|$ exists, it is used as the initial condition for the next Re-value.

3.2. *Boundary conditions*

The problem involves two driving forces: buoyancy acting as a body force in the bulk and thermocapillarity acting on the upper surface of the fluid. The dynamical boundary condition on this upper surface relates the velocity gradient to the temperature gradient through the following dimensionless formula (see Birikh 1966):

$$\frac{\partial v}{\partial x} = \frac{Re}{Gr^{\frac{1}{2}}}\frac{\partial \theta}{\partial y}; \tag{4}$$

the other conditions on the horizontal boundaries are

$$v(0, y) = u(0, y) = 0; \quad u(1, y) = 0; \tag{5}$$

and

$$\theta(0, y) = \theta(1, y) = A - y \tag{6a}$$

for the conducting case; and

$$\frac{\partial \theta}{\partial x}(0, y) = \frac{\partial \theta}{\partial x}(1, y) = 0 \tag{6b}$$

for the insulating case.

When the condition (6*a*) applies, the vorticity at the free surface is constant. The boundary conditions on the rigid vertical walls are

$$\theta(x,0) = A\,; \quad \theta(x,A) = 0,$$

and

$$u(x,0) = v(x,0) = u(x,A) = v(x,A) = 0.$$

The effect of interface deformability on the onset of instability has not been investigated but its influence on the flow velocity has been given by Strani *et al.* (1983) for the steady-state regime at relatively low Reynolds numbers. The shape of the gas–liquid interface in a square cavity has been computed by Cuvelier & Driessen (1986) for different values of driving forces. For pure buoyancy flow, the pressure is higher in the upper hot corner. Consequently, there is an elevation of the free boundary in this corner and a depression near the cold corner. For pure thermocapillary flow, an opposite effect is observed. For combined convections the free surface is flattened by increasing the (positive) Bond number, $Bo = g\rho_0 L^2/\sigma_0$. Cuvelier & Driessen also showed that the free-surface shape strongly depends on the Ohnesorge number ($Oh = \mu/(\rho_0 \sigma_0 L)^{\frac{1}{2}}$). When Oh is small (e.g. 0.05) the free surface is nearly horizontal. For larger Oh, distortion is less and less negligible. But for liquid metals, the surface-tension coefficient σ_0 is generally high and thus Oh is small.

In the above formulation (1)–(4), the free-surface deformation is neglected. This assumption is valid in crystal growth applications with small capillary (Ohnesorge) numbers and 90° contact angles between the vertical solid wall and the meniscus.

4. Numerical procedure

The governing equations (1)–(3) are solved using an ADL (alternating direction implicit) technique with a finite-difference method involving forward differences for time derivatives and Hermitian relationships for spatial derivatives with a truncation error of $O(\Delta t^2, \Delta x^4, \Delta y^4)$ (see Hirsh 1975; Roux *et al.* 1979). Boundary vorticity was updated with an equation exhibiting fourth-order accuracy. The derivation of the discretized equations for the two-dimensional problem is not given here but it follows the approach described in Roux *et al.* (1979) and Ben Hadid (1989). A block tridiagonal matrix inversion algorithm (Thomas algorithm) is employed for the finite-difference form of (1)–(3). The convergence criterion for the Navier–Stokes equations is based on the local vorticity (maximum relative variation of vorticity less than 0.01 %).

In order to accurately describe gradients in boundary layers which develop with thickness $\delta \sim Re^{-\frac{1}{3}}$ at large Re (Ben Hadid *et al.* 1988), it is necessary to use a non-uniform grid in the x-direction. A non-uniform grid is also needed in the y-direction since the flow is asymmetric even at moderate Grashof and Reynolds numbers. Previous simulations of two-dimensional buoyancy-driven convection demonstrated the importance of grid resolution. In particular, for low-Prandtl-number fluids, it was found that a coarse grid in the boundary regions delayed the onset of oscillatory regimes. Thus, grid refinement is needed near the boundaries and in the 'vortex region' which develops in the vicinity of the endwalls depending on the relative strength of thermocapillary and buoyancy flows. Such a grid refinement is achieved by using the coordinate transformation proposed by Thompson, Thames & Mastin (1974).

The accuracy of the results was assessed by increasing the number of grid points in each spatial direction. For example, some flow characteristics such as the mean

Gr	Grid size	$\overline{\psi_{max}}$	$\dfrac{\overline{\Delta\psi_{max}}}{\overline{\psi_{max}}}$	f
	25×81	0.5948	—	—
1.5×10^4	31×91	0.5975	—	—
	41×121	0.5960	—	—
	25×81	0.6473	14.86	24.40
4×10^4	31×91	0.6503	15.37	24.20
	41×121	0.6500	15.10	24.15
	25×81	0.6565	16.14	31.32
6×10^4	31×91	0.6597	16.53	31.12
	41×121	0.6573	16.46	31.05

TABLE 1. Accuracy tests for $A = 4$, $Re = 0$ and insulated horizontal boundaries

value of the maximum of the stream function, $\overline{\psi_{max}}$, its rate of fluctuation, $\overline{\Delta\psi_{max}}/\overline{\psi_{max}}$, and the oscillation frequency, are presented in table 1, for $A = 4$ and $Re = 0$. Comparisons between a 31×91 and a 41×121 variable grid show that 31×91 grid is sufficient for an accuracy of better than 0.3% for $\overline{\psi_{max}}$ and frequency f. The 31×91 grid is built in such a way that the ratio between the smallest step of a variable grid and that of a uniform grid is of order 4 at the cold corner and of order 2 at the hot corner (for $Re > 0$); the grid spacing is gradually increased away from the boundaries. An opposite stretching is used for $Re < 0$, with larger grid refinement at the hot corner.

The effect of the grid has also been investigated for large aspect ratios. For $A = 12.5$ a non-uniform 31×201 grid (with local refinement near the endwalls) was used for the steady asymmetric flows as well as a uniform 31×251 grid for some cases (mainly for unsteady flows). For $A = 25$, the majority of solutions reported in this paper were obtained with a non-uniform 31×251 grid for steady flows and a uniform 31×401 grid for unsteady flows.

The results of numerical experiments carried out for shallow cavities are described hereinafter; the prominent effects of the governing parameters (e.g. Gr, Re and A) on the flow structure will be illustrated by contour plots of streamlines and isotherms in the steady-state cases, and by iso-ψ plots and time histories of some characteristic quantities in the unsteady cases. The influence of the Grashof number for purely buoyancy-driven (oscillatory) flows will be presented in §5.1 for $A = 4$. A discussion of the effect of both negative and positive Reynolds numbers will be presented for $A = 4$ (in §5.2) and for $A = 12.5$ and 25 (in §5.3). The steady-state flow structure which prevails for high $|Re|$ will be discussed in §6 for both opposing and additive cases.

5. Unsteady flow results (small $|Re|$)

5.1. *Pure buoyancy-driven flows for moderate aspect ratio, $A = 4$*

The influence of natural convection on the flow when thermocapillary forces are absent is considered here. By setting $Re = 0$, the right hand side of (4) vanishes and thus the vorticity at the surface is constant and equal to zero. In a previous work, Ben Hadid & Roux (1990*a*) used Hermitian finite-difference methods to investigate

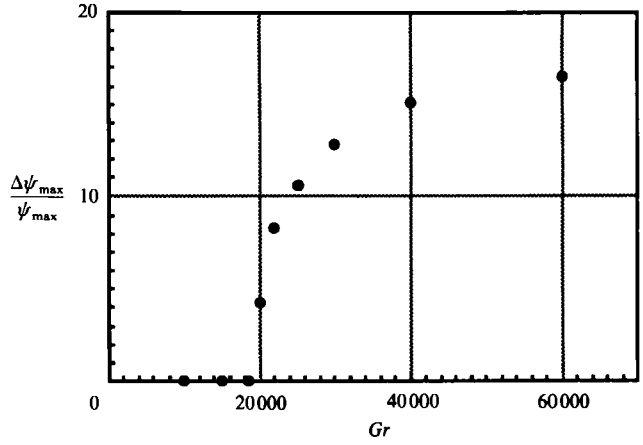

FIGURE 2. Pure buoyancy convection for $A = 4$ and insulated horizontal walls: the relative amplitudes of ψ_{max} for several Grashof numbers.

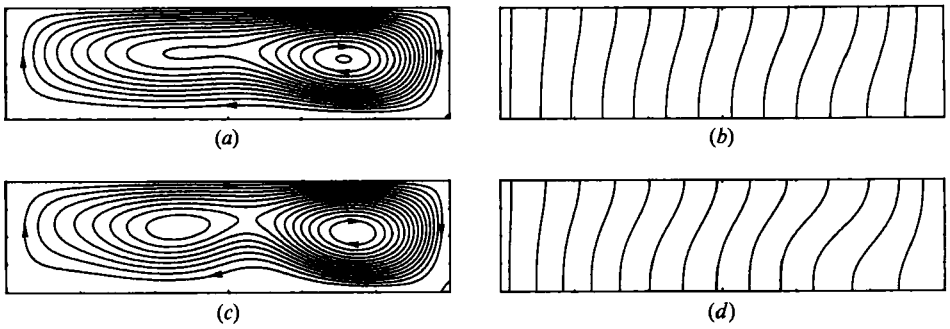

FIGURE 3. Steady solutions in the pure buoyancy-convection case for $A = 4$; (*a*) streamline patterns and (*b*) isotherms at $Gr = 6 \times 10^3$; (*c*) streamline patterns and (*d*) isotherms at $Gr = 6 \times 10^3$.

the structure of the oscillatory flow regimes in a cavity with moderate aspect ratio $A = 4$ and conducting horizontal boundaries. For $Pr = 0.015$ the authors noted that for small Grashof numbers ($Gr < 5 \times 10^3$) a vortex progressively forms in the cold region leading to an asymmetric cellular flow. On further increasing Gr, a stationary bifurcation is reached with the appearance of a secondary cell followed by a transition to unsteady flow. A periodic flow occurs for $Gr_c \approx 1.5 \times 10^4$ and persists for higher Gr (see §2.1).

For insulating horizontal boundaries the transition to a periodic flow occurs for $Gr_c \approx 1.9 \times 10^4$. This result agrees with those in the literature (see Winters 1988; Pulicani 1989). At $Gr = 1.95 \times 10^4$ the amplitude of the fluctuations increases very slowly; it is only 0.64% after 1.18 viscous time ($t_\nu = t\nu/H^2$) units. Then, the dimensionless frequency calculated from the maxima of ψ_{max} is close to 15. Since we initiate the solution from a steady-state condition and wait until the flow eventually reaches its stable oscillatory state, the length of the transient state increases drastically as the bifurcation point is approached. Calculations were carried out over 0.7, 1.4 and 3.3 viscous time units to obtain a constant amplitude of oscillation for $Gr = 2.5 \times 10^4$, 2.2×10^4 and 2×10^4, respectively. The relative amplitude of ψ_{max} for various Grashof numbers near the critical point (Hopf bifurcation) is displayed in figure 2.

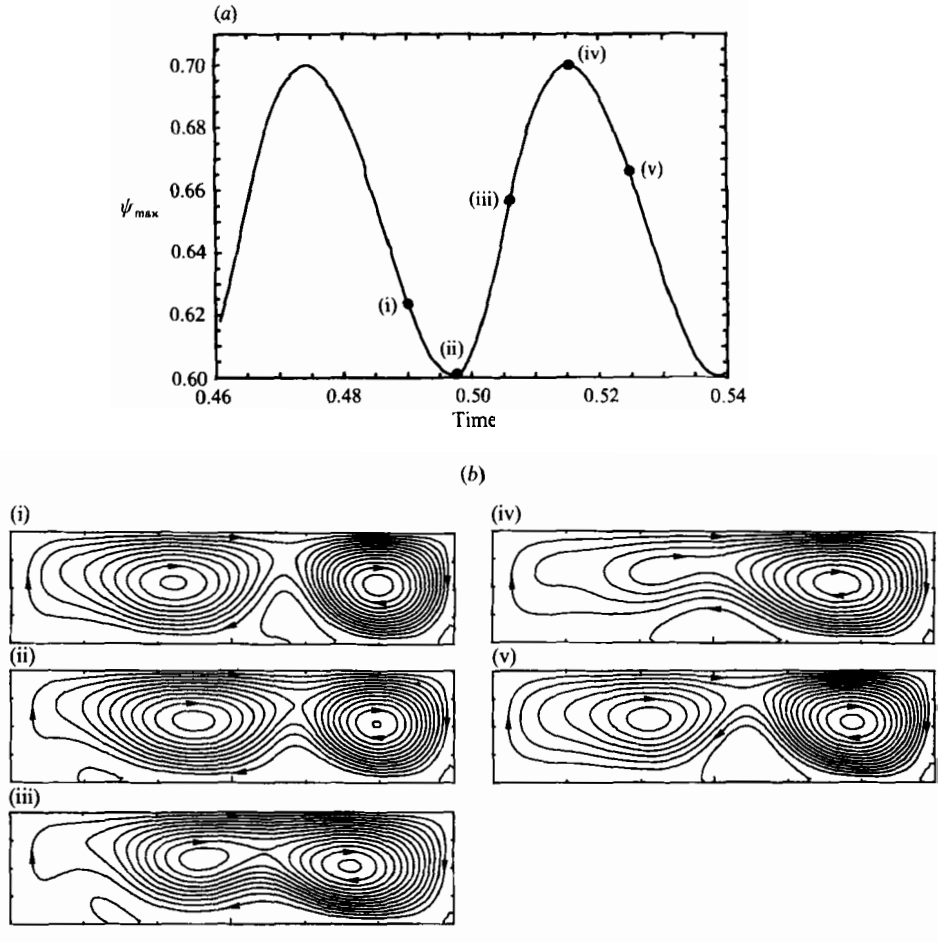

FIGURE 4. (*a*) Time history of ψ_{max} for $A = 4$ and $Gr = 4.10^4$. (*b*) Time-dependent solutions in the pure buoyancy-convection case shown in (*a*). the iso-ψ lines correspond to time values (i)–(v) in (*a*). The contour levels range from ψ_{max} and zero in equal steps.

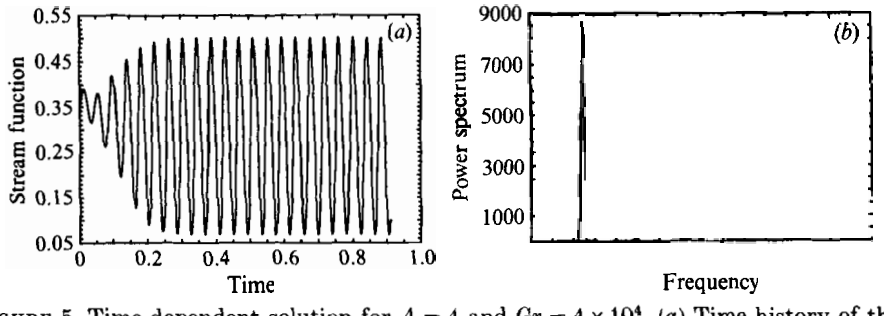

FIGURE 5. Time-dependent solution for $A = 4$ and $Gr = 4 \times 10^4$. (*a*) Time history of the stream function at $x = 0.5$ and $y = \frac{1}{2}A$, (*b*) its power spectrum.

The qualitative features of steady flows are shown in figures 3(*a*) and 3(*c*) for two values of Gr below the onset of unsteady flow ($Gr = 6 \times 10^3$ and 1.5×10^4). In these figures the flow circulates from left to right (from hot to cold) at the upper surface and the loss of flow symmetry is due to the loss of symmetry in dynamical boundary

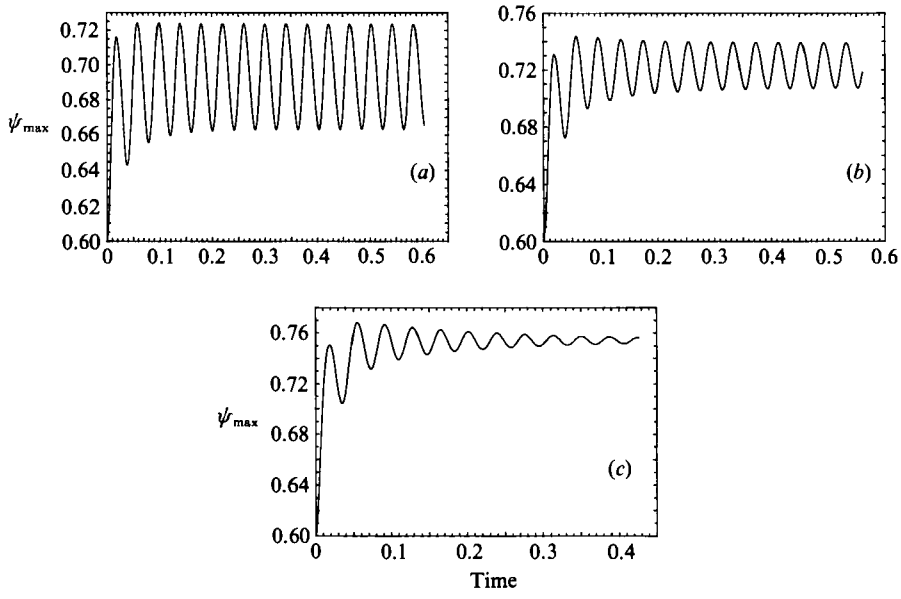

FIGURE 6. Time-dependent solutions in the additive case for $A = 4$ and $Gr = 4 \times 10^4$. Time history of ψ_{max} for three Reynolds numbers: (*a*) $Re = 6 \times 10^2$, (*b*) $Re = 1.2 \times 10^3$ and (*c*) $Re = 2 \times 10^3$.

conditions (bottom surface is rigid while the upper is stress-free). The flow structure exhibits the onset of a secondary stationary vortex (the primary one being in front of the cold wall) for $Gr \approx 6 \times 10^3$. For higher Gr the strength of the two vortices increases and a weak counter-rotating vortex appears near the bottom wall between the primary and secondary vortices.

An additional increase of Gr leads to an increase of the amplitude of the time-dependent flow fluctuations. This evolution is continuous (see figure 2) and, for example, periodic fluctuations with a constant amplitude are attained after nearly 0.3 viscous time units, for $Gr = 4 \times 10^4$. Figure 4(*a*) displays a portion of the time history, and the flow structures corresponding to those points over a period identified in figure 4(*a*) are represented through iso-ψ lines in figure 4(*b*). The sequence of iso-ψ lines (figure 4*b*) shows a periodic change of vortex shape (expansion and contraction) and reveals that the two main vortices (primary and secondary) intensify and create two reverse flows (counter-rotating) which are periodically created and destroyed.

A more quantitative examination of flow fluctuations throughout the cavity reveals that the fluctuations increase from the bottom towards the upper surface and reach their maximum amplitude in the middle part of the cavity ($y = \frac{1}{2}A$). The behaviour of the fluctuations is illustrated by the time history of $\psi(x = 0.5, y = A/2)$ in figure 5(*a*). The corresponding power spectrum in figure 5(*b*) exhibits one frequency peak, indicating that this oscillatory flow is simply periodic $P^{(1)}$.

5.2. *Combined buoyancy and thermocapillary forces for* $A = 4$

With combined buoyancy and thermocapillary forces two cases will be examined: an additive ($Re > 0$) or opposing ($Re < 0$) effect. Previously, it was stated that the thermocapillary force can significantly affect the dynamics of the instability in such a manner that oscillatory flow induced by buoyancy forces can be damped (inverse

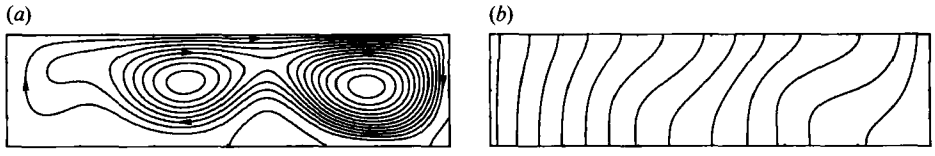

FIGURE 7. Steady-state solution in the additive case for $A = 4$, $Gr = 4 \times 10^4$ and $Re = 2 \times 10^3$; (a) streamline patterns and (b) isotherms.

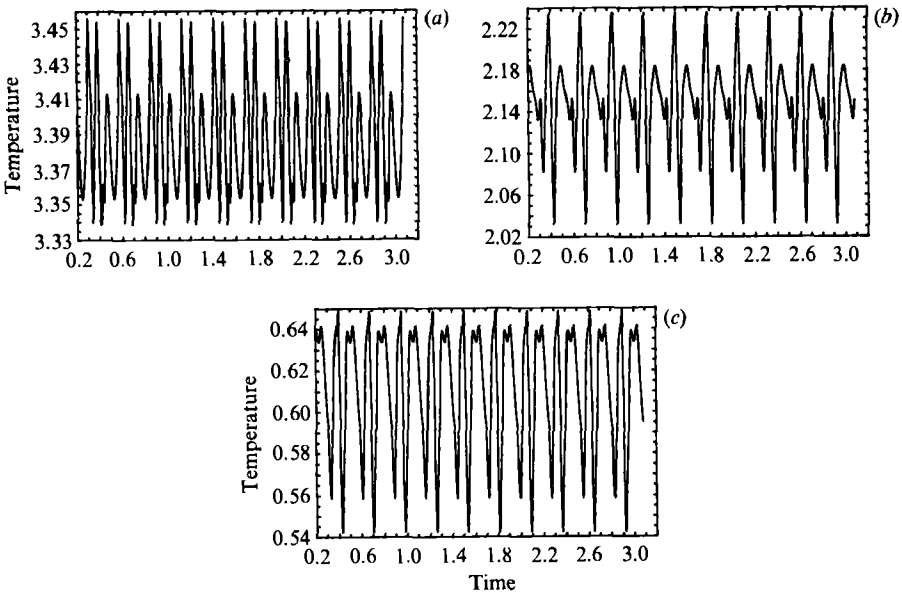

FIGURE 8. Time-dependent solutions for $A = 4$, $Gr = 4 \times 10^4$ and $Re = -2 \times 10^3$. Time history of surface temperature at three horizontal locations: (a) $y = \frac{1}{4}A$, (b) $y = \frac{1}{2}A$ and (c) $y = \frac{3}{4}A$.

bifurcation) when $|Re|$ exceeds a certain critical value. The first example here is for the 'additive case' at $Gr = 4 \times 10^4$: for $Re = 600$ the solution quickly resumed a time-periodic behaviour after some initial transient which is a consequence of a sudden change in the value of Reynolds number (figure 6a). The amplitude of $\psi_{\max}$ of the periodic motion is about 8.73% of the mean value $\overline{\psi_{\max}}$, and the dimensionless frequency was $f = 27$. For $Re = 1.2 \times 10^3$ and 2×10^3 (figure 6b and 6c) the evolution of $\psi_{\max}$ over time clearly shows that the amplitude of the oscillatory flow diminishes with increasing Re; it is 4.5% of the mean value $\overline{\psi_{\max}}$ for $Re = 1.2 \times 10^3$. Upon further increasing the Reynolds number to $Re = 2 \times 10^3$ the flow reverts to a steady state after several damped oscillations. Inspection of figure 7 reveals that there is no drastic change in the flow structure with respect to the steady, purely buoyancy-driven flow (e.g. $Re = 0$, in figure 3) apart from an increase of the mean flow rate given by $\overline{\psi_{\max}} \approx 0.758$. Inspection of the corresponding thermal field indicates that in the region of the hot wall the isotherms are nearly straight (the small noticeable distortion of the isotherms can easily be linked to the cellular flow).

Obviously the coupling is expected to be more intricate in the 'opposing case'. In this case we observe that for $Gr = 4 \times 10^4$ the flow remains unsteady with a complicated time behaviour in a certain small range of negative Re. In this narrow range of Re there is a rapid change in the flow regime which evolves from a periodic state to a bi- or quasi-periodic state when the Reynolds number is varied from

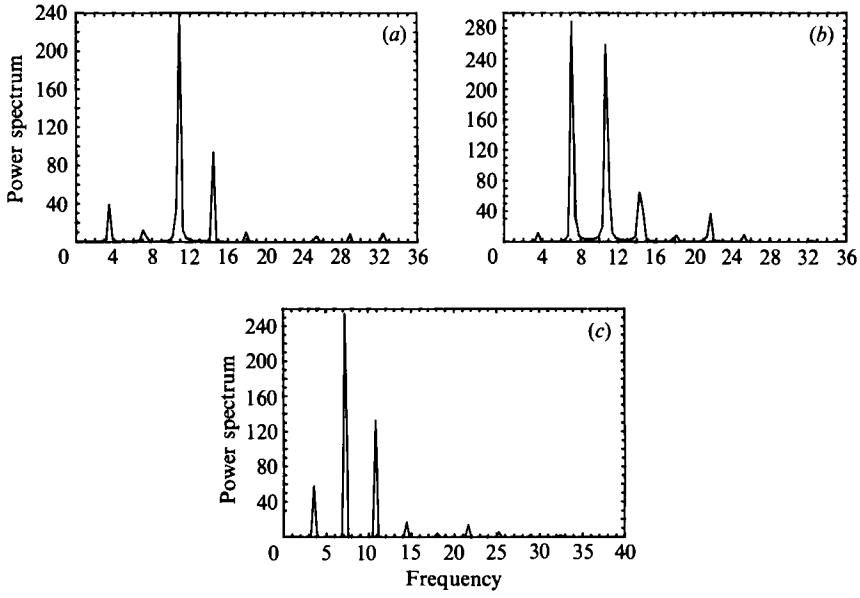

FIGURE 9. As for figure 8 but showing the temperature power spectra as a function of frequency.

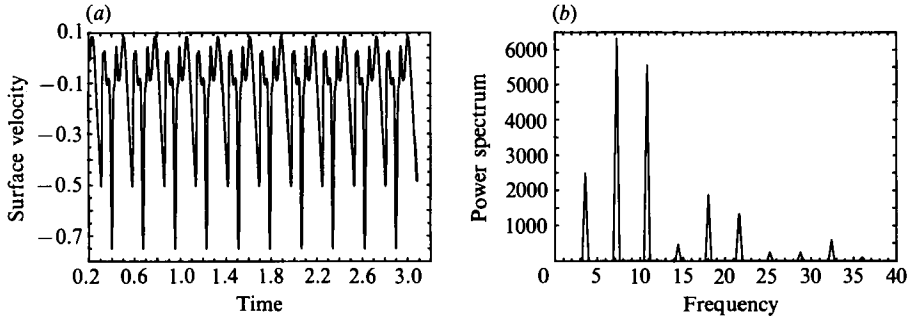

FIGURE 10. as for figure 8 but showing the surface velocity at $y = \frac{1}{2}A$, (*a*) time history, (*b*) its power spectrum.

$Re = -10^3$ to -2×10^3. For $Re = -10^3$ the computation was started from an established purely buoyancy-driven oscillatory solution at $Gr = 4\times10^4$ and $Re = 0$. The solution remained unsteady with oscillation amplitudes of ψ_{max} of about 23.3% of its mean value ($\overline{\psi_{max}}$) and with a frequency of $f = 16.38$. When Re is further decreased ($Gr = 4\times10^4$ and $Re = -2\times10^3$) the system evolves to a somewhat more complex time-dependent regime. The flow at $Re = -2\times10^3$ is no longer simple periodic, as evident in the time-history plot of the surface temperature for three horizontal locations $y = \frac{1}{4}A$, $\frac{1}{2}A$ and $\frac{3}{2}A$ presented in figures 8(*a*), 8(*b*) and 8(*c*), respectively, and their corresponding power spectra in figures 9(*a*), 9(*b*) and 9(*c*). This behaviour is confirmed by that of the surface velocity at $y = \frac{1}{2}A$, presented in figure 10(*a*) with its density power spectrum in figure 10(*b*). Several new features are seen in these figures. The flow is characterized by two distinct frequencies: $f_1 = 10.75$ and $f_2 = 7.22$. As remarked by one of the reviewers the ratio f_2/f_1 is close to 2/3 (so it is not possible to directly conclude that the regime is bi- or quasi-periodic). A supplementary peak corresponding to $f' = 3.36$ (i.e. $f' \approx f_1 - f_2$, or $f' \approx \frac{1}{2}f_2$) is observed

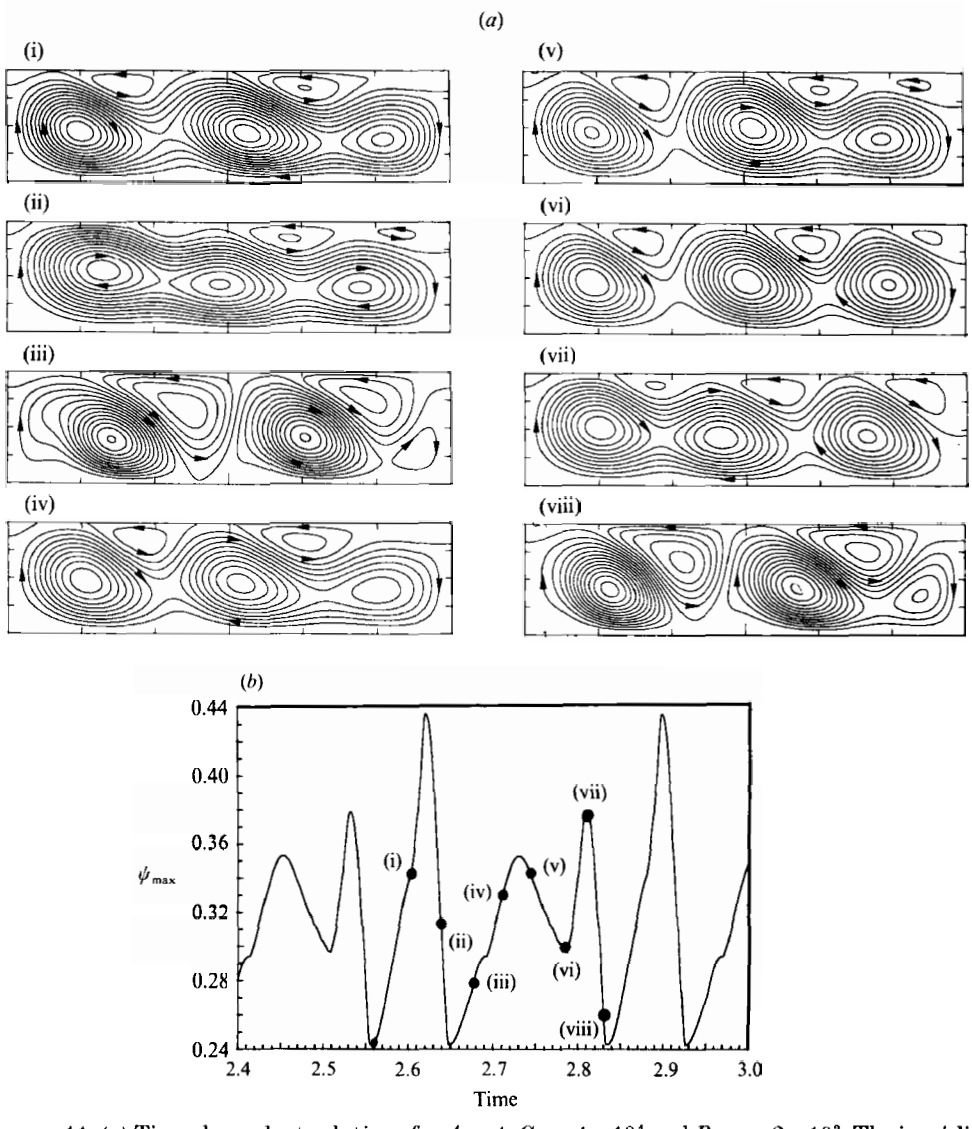

FIGURE 11. (*a*) Time-dependent solutions for $A = 4$, $Gr = 4 \times 10^4$ and $Re = -2 \times 10^3$. The iso-ψ lines corresponding to time values (i)–(viii) in (*b*). The contour levels range from ψ_{max} and zero in equal steps. (*b*) As for (*a*) but showing the time history of ψ_{max}.

in the density power spectrum. The same frequencies are observed at different positions in the flow fields but the amplitudes of the spectral components vary with location. In particular, the amplitude of f_2 is small for $y = \frac{1}{4}A$ (figure 9*a*) and rapidly increases for $y \geqslant \frac{1}{2}A$ (figure 9(*b*, *c*). It is therefore difficult to characterize the flow field by only one time-behaviour recorded at one fixed point. The calculated relative amplitude of the fluctuations of ψ_{max} of this bi- or quasi-periodic motion is about 54.8 %, which is much larger than that for a purely buoyancy-driven flow. The effect of these strong fluctuations is also visible on the time variations of the flow structure shown at eight instants over a period in figure 11(*a*) (instants (i)–(viii) are displayed in the time-history segment of ψ_{max} in figure 11(*b*). The opposing forces generate counter-rotating vortices at the surface which periodically grow and even split the

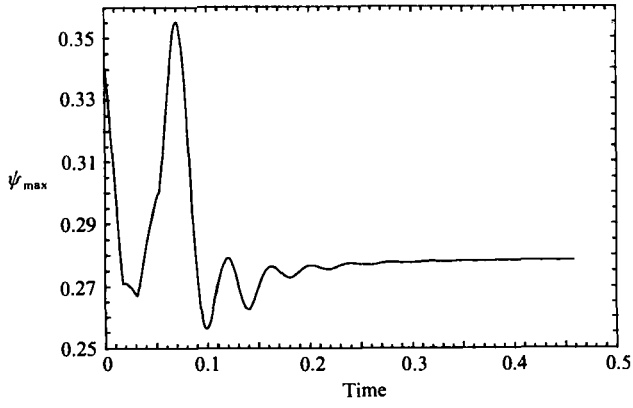

FIGURE 12. Time history of ψ_{max} for $A = 4$, $Gr = 4 \times 10^4$ and $Re = -2.4 \times 10^3$.

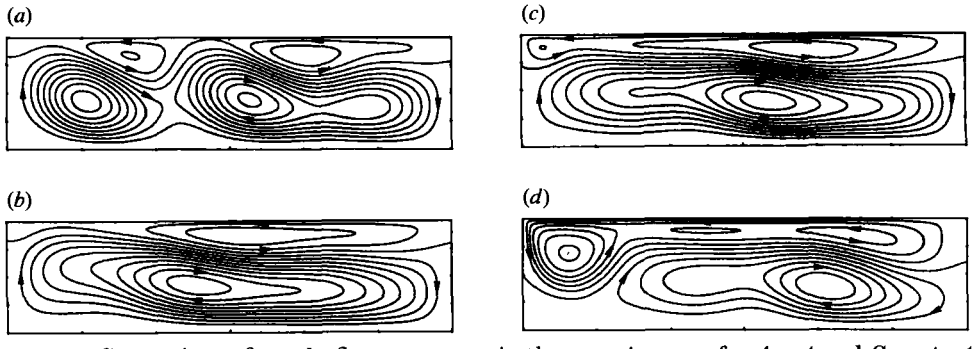

FIGURE 13. Comparison of steady flow structures in the opposing case for $A = 4$ and $Gr = 4 \times 10^4$. Streamline patterns for: (*a*) $Re = -2.4 \times 10^3$, (*b*) $Re = -3 \times 10^3$, (*c*) $Re = -4 \times 10^3$ and (*d*) $Re = -6.667 \times 10^3$.

flow (instants iii and viii). Despite the decrease of mean flow rate (e.g. $\overline{\psi_{max}}$), the flow structure becomes more complex with an increase of oscillation amplitude and a decrease of frequency.

Using an instantaneous solution obtained for $Gr = 4 \times 10^4$ and $Re = 0$ as initial condition, and further decreasing Reynolds number down to $Re = -2.4 \times 10^3$, the solution ψ_{max} starts to oscillate with a large overshoot and undershoot (see figure 12); then oscillations are rapidly damped and the solution converges to a steady state. The structural feature of this steady-state solution is the presence, close to the upper boundary, of two counter-rotating vortices generated by the thermocapillary flow. Note that the reverse transition from an unsteady to a steady solution is not directly linked to disappearance of the multicellular flow structure close to the upper boundary and within the cavity. The solutions obtained for increasingly negative Re ($Re = -6.67 \times 10^3$) rapidly converge to a steady state and show that the two counter-rotating vortices present at $Re = -2.4 \times 10^3$ coalesce and form a counter-rotating vortex which extends over the length of the cavity (see figures 13*b* and 13*c*). With further decreasing Re ($Re = -6.67 \times 10^3$) the top cell expands and spreads towards the hot vertical wall (figure 13*d*). In figure 13 it is also clear that there is a progressive reduction of size and strength of the buoyancy vortex in the lower part of the cavity. For $Re = -4 \times 10^3$ the steady solution is indeed characterized by two superposed vortices, the upper only mainly driven by thermocapillarity and the lower one by

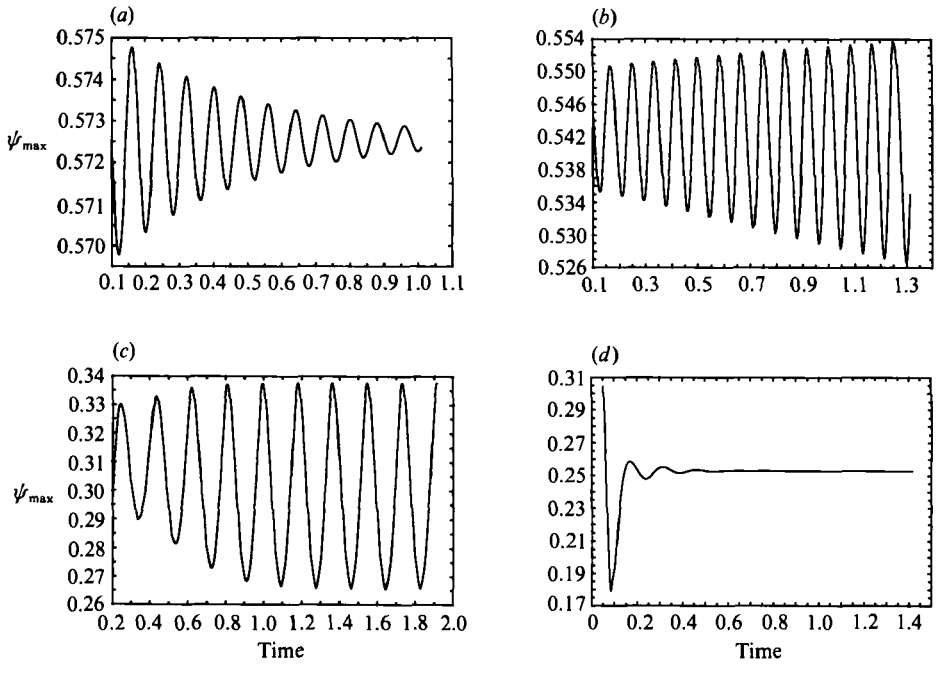

FIGURE 14. time history of ψ_{max} in the opposing case for $A = 4$, $Gr = 1.5 \times 10^4$ and several negative Reynolds numbers: (*a*) $Re = -2 \times 10^2$, (*b*) $Re = -4 \times 10^2$, (*c*) $Re = -10^3$ and (*d*) $Re = -1.2 \times 10^3$.

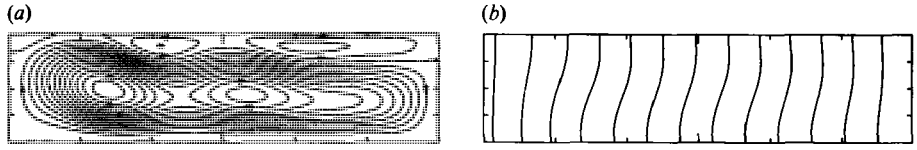

FIGURE 15. Steady solution in the opposing case for $A = 4$, $Gr = 1.5 \times 10^4$ and $Re = -1.2 \times 10^3$: (*a*) streamline patterns and (*b*) isotherms.

buoyancy force. The same trends showing two vortices in the top left and right corners that coalesce at higher $|Re|$ have been previously reported for an aspect ratio $A = 2$ by Villers & Platten (1987*b*), and for $A = 4$ by Villers (1989) for $Pr = 4$.

As a result of numerous computations for various negative Re-values, we conclude that the critical Grashof number for the onset of an oscillatory instability substantially decreases in the 'opposing case'. This is illustrated in figure 14 where the time evolution of ψ_{max} for $Gr = 1.5 \times 10^4$ and $Re = -200$, -400, -10^3 and -1.2×10^3 are shown. The flow remains steady for small $|Re|$ ($Re = -200$, figure 14*a*), while an oscillatory instability occurs in a certain range of negative Re (figure 14*b*, *c*). As is readily observed in other circumstances ($Gr = 4 \times 10^4$ and $Re = -2.4 \times 10^3$), the flow is no longer oscillatory when Re is further decreased ($Re = -1.2 \times 10^3$, figure 14*d*). So, a reverse transition to a steady flow occurs in the range $-1.2 \times 10^3 < Re < -10^3$. The steady-state flow structure at $Re = -1.2 \times 10^3$ is shown in figure 15(*a*). As in figure 13(*a*) for $Bd = -16.66$, the flow structure in figure 15(*a*) for $Bd = -12.5$ shows counter-rotating vortices which indicate dominance of thermocapillary force near the upper free surface. Figure 15(*b*) shows that the isotherms

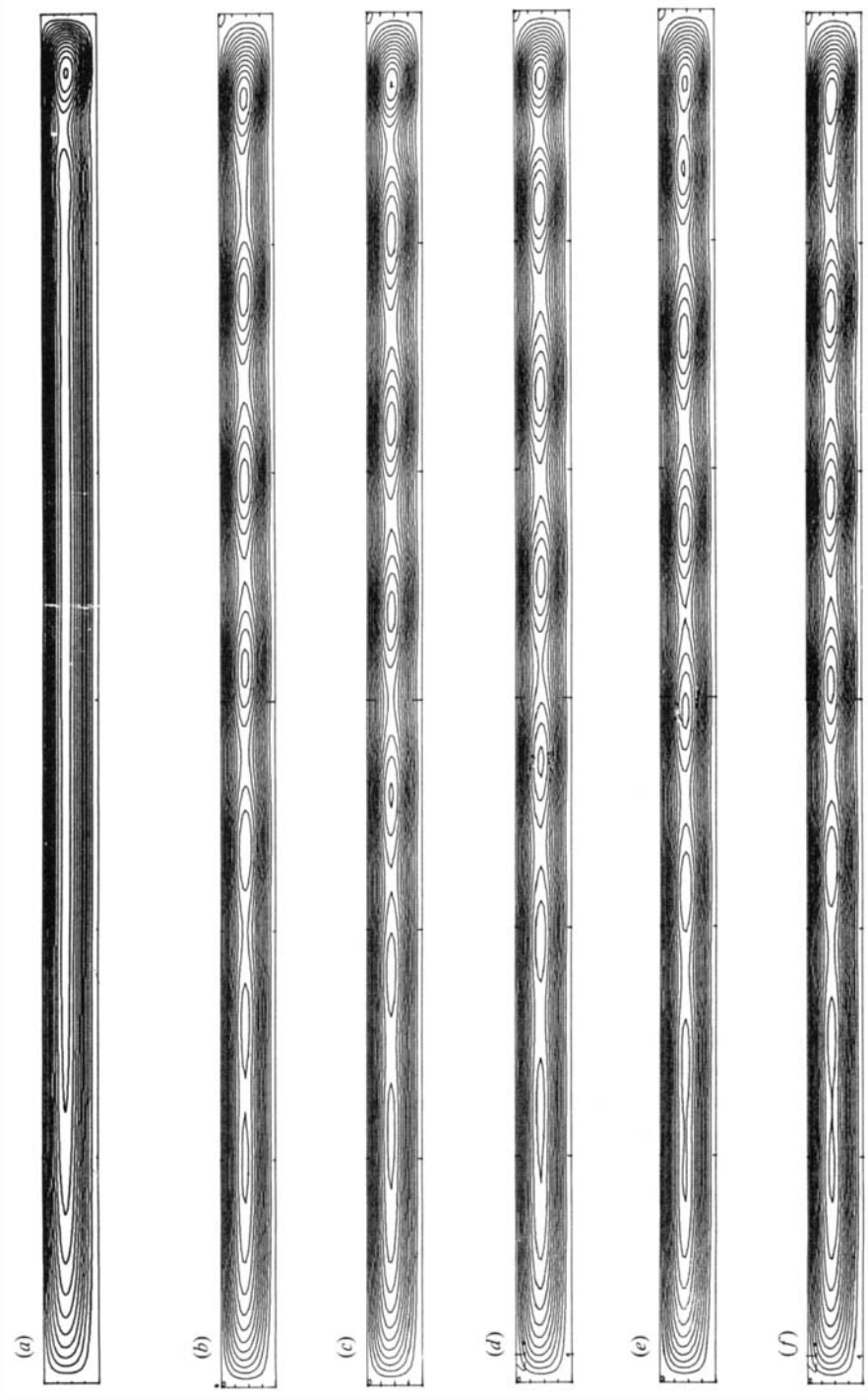

FIGURE 16. Flow pattern for $A = 25$ and $Gr = 6 \times 10^3$: (*a*) streamlines at $Re = 0$, (*b–f*) instantaneous iso-ψ lines corresponding to the time values in figure 17 for the time-dependent solutions in the opposing case at $Re = -2 \times 10^2$.

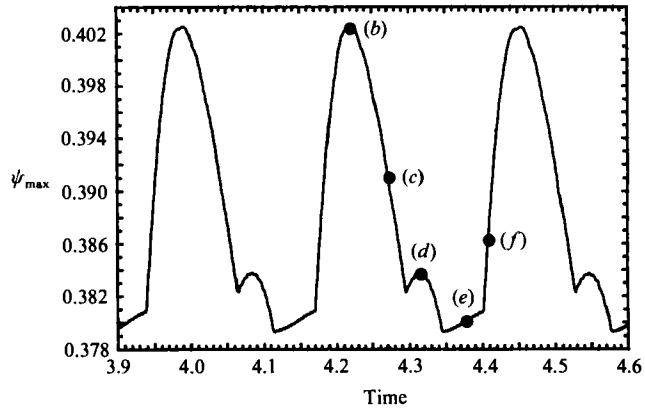

FIGURE 17. As figure 16 showing time history of ψ_{max}. the symbols (*b–f*) correspond to values of time at which the iso-ψ lines are given in figure 16(*b–f*).

are slightly distorted in the vortex regions and remain nearly straight in the vicinity of the vertical walls.

5.3. *Higher aspect ratios*: $A = 12.5$ *and* 25

For $A = 25$ and $Gr = 6 \times 10^3$ the purely buoyancy-driven flow is steady as expected (figure 16*a*). The flow pattern is asymmetric and dominated by a single cell in front of the cold wall. This asymmetric monocellular solution was used as initial condition to carry out the solutions for more negative Reynolds numbers. The steady-state regime appears to be maintained from $Re = 0$ to roughly $Re \approx -200$ where a transition to a time-dependent state occurs. The spatial structure of this oscillatory flow can be analysed by looking at the iso-ψ lines at equally spaced instants in figure 16*b–f*). A typical time history of ψ_{max} is displayed for $Re = 200$ in figure 17. Calculations have been carried out for a time long enough to reach the regime of constant amplitude fluctuations. Each frame of figure 16 exhibits a global circulation along the horizontal walls flowing from left to right (from hot to cold) at the top of the cavity and in the opposite sense at the bottom. Also several internal cells affecting the middle region (midplane) of the cavity are apparent in the figure. During a cycle, a seven-cell pattern is evident and the cells move from left to right; a new cell is created near the hot side (figures 16*e* and 16*f*), while in the cold region the cells move close together until they merge (figure 16*e*). The internal cells result from the shear between two main opposite streams. Their strength is clearly non-uniform along the horizontal upper surface; it is weaker in the hot region and becomes stronger as the cells move towards the cold wall. The number of internal cells filling the cavity varies between seven and eight during one cycle, owing to generation or collapse of cells in the end regions. Unsteady solutions displaying similar characteristics are also found for a large thermocapillary effect, e.g. for $Re = -300$. A further decrease of Re eventually yields a steady multicellular flow (for $Re \approx -500$). For even smaller Re, a stronger restabilization is observed.

The relative amplitude of the fluctuation of ψ_{max}, $\Delta\psi_m = \Delta\psi_{max}/\overline{\psi_{max}}$, is 6.14% for $Re = -200$ with a dimensionless frequency of $f = 4.32$. The fluctuation amplitude and frequency are found to decrease with Reynolds number (i.e. $\Delta\psi_m = 2.4\%$ and $f \approx 2.38$ for $Re = -300$). Furthermore, the time evolution of the stream function through the cavity shows that the fluctuation amplitude continuously increases from left to right. The time history of the stream function at $x = 0.5$ is plotted in figures

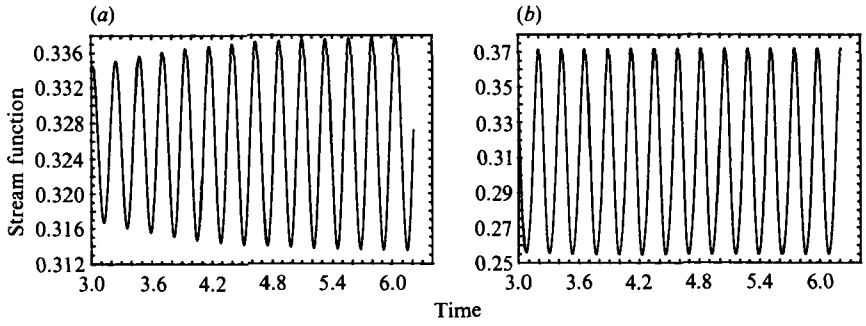

FIGURE 18. Time-dependent solutions in the opposing case for $A = 25$, $Gr = 6 \times 10^3$ and $Re = -2 \times 10^2$. Time history of the stream function at two locations in the horizontal centreline: (*a*) $y = \frac{1}{4}A$ and (*b*) $y = \frac{3}{4}A$.

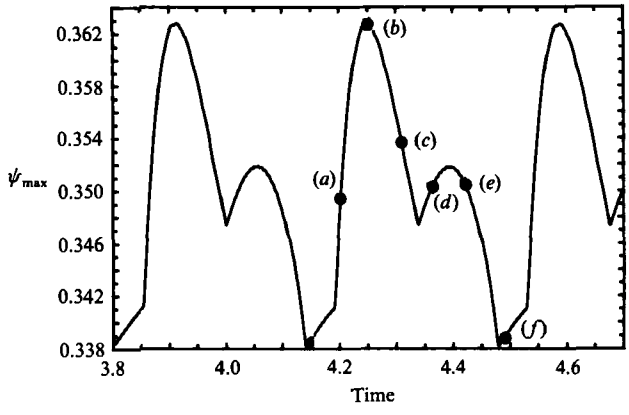

FIGURE 19. Time-dependent solution in the opposing case for $A = 12.5$, $Gr = 6 \times 10^3$ and $Re = -266$. Time history of ψ_{max}. The symbols (*a*)–(*f*) correspond to values of time at which the iso-ψ lines are given in figure 20.

18(*a*) and 18(*b*) for two locations corresponding to $y = \frac{1}{4}A$ and $\frac{3}{4}A$, respectively; these plots show that the relative amplitude of the fluctuations with respect to the local average value is approximately five times larger at $y = \frac{3}{4}A$ than at $y = \frac{1}{4}A$.

For $A = 12.5$ and $Gr = 6 \times 10^3$ steady flow solutions were obtained for Re values down to -200. An unsteady multicellular flow results at $Re = -233$ starting from the steady solution for $Re = -200$ as initial condition. When the Reynolds number is decreased to -266, the solution is again unsteady; we observe the development of the instability and its evolution to a time-periodic solution. Finally, when the Reynolds number is set to $Re = -300$, a reverse transition occurs leading to a steady-state solution. Therefore, the onset of the unsteady flow is restricted to a narrow range of negative Re: $-300 < Re < -200$.

Figure 19 illustrates the time evolution of ψ_{max} fluctuations for $Re = -266$. At the onset of unsteady flow the motion is typically time-periodic with a simple period. With decreasing Re, the amplitude of ψ_{max} fluctuations becomes weaker ($\Delta\psi_m = 9\%$ for $Re = -233$ and $\Delta\psi_m = 7\%$ for $Re = -266$). The structure of the unsteady flow is illustrated in figure 20 in which a time history of the stream function is shown at six instants over one period. A characteristic flow property at $Re = -266$ is a large cell in the left part and a cell with stronger circulation which is seen to coalesce with an adjacent one near the cold wall. Near the hot wall a large cell arises and moves

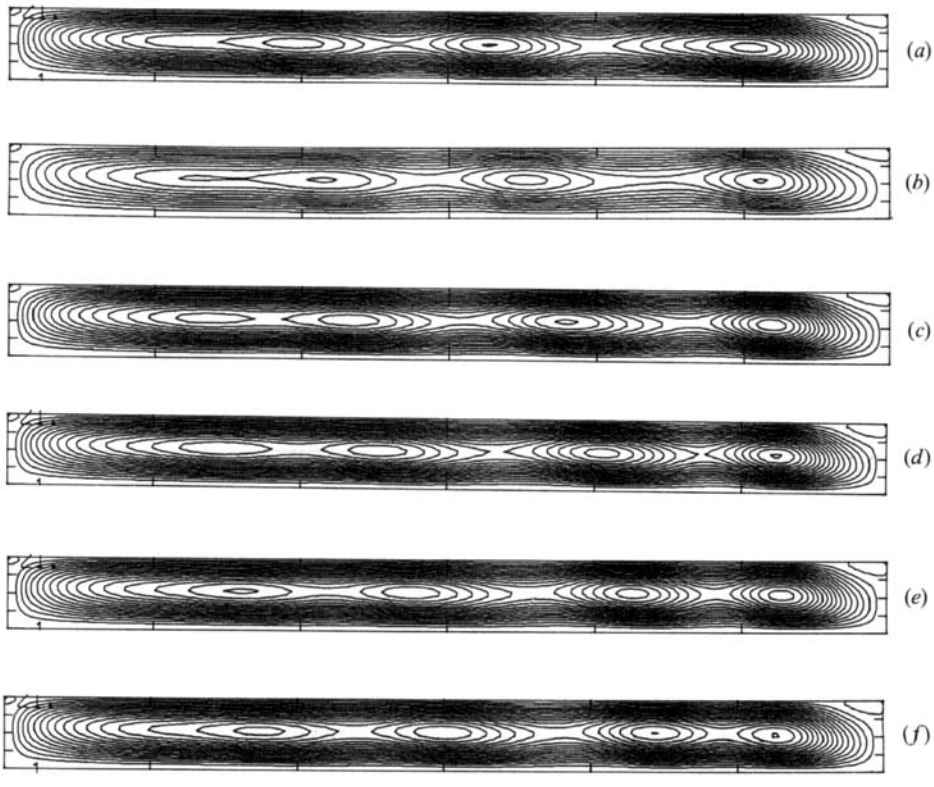

FIGURE 20. As figure 19 but showing instantaneous iso-ψ lines: (*a*)–(*f*) correspond to time values in figure 19. The contour levels range from ψ_{max} and zero in equal steps.

towards the cold wall. Because the thermocapillary force exceeds the buoyancy force a tiny convective recirculation develops in the two upper corners. A qualitatively similar unsteady regime is obtained at $Re = -233$.

We also note that the oscillation frequency decreases with decreasing Re; this phenomenon is also observed with $A = 25$. The oscillation frequency is about $f = 3.67$ and 2.96 in terms of viscous time units for $Re = -233$ and -266, respectively. It is noteworthy that for $Gr = 6 \times 10^3$ the frequency varies linearly with Re as shown in figure 21 where the dots represent the computed values in the domain $-300 \leqslant Re \leqslant -200$ for $A = 25$ and 12.5, and where solid line represents the linear relationship: $f = a + b \times Re$, with $a = 8.23$ and $b = 0.02$.

A theoretical study of an infinite horizontal layer by Laure & Roux (1989) has shown that the two-dimensional perturbation corresponds to a travelling wave propagating along the y-axis. Graphical evaluation of the non-dimensional wavelength in the central region of the cavity from the plot of the iso-ψ lines for $Gr = 6 \times 10^3$ yields 3.35 ± 0.25 and 3.24 ± 0.25 at $Re = -200$ and $Re = -300$, respectively. These values compare favourably to those obtained from the stability analysis of P. Laure (1989, private communication), 3.248 and 2.802 for $Re/Gr = -0.033$ and 0.050, respectively. The non-dimensional wave speed is defined as $c = c^* H/\nu$, where c^* is the dimensional wave speed. The values of c are 14.70 ± 1.20 and 8.16 ± 1.16 at $Re/Gr = -0.033$ and -0.050, respectively; they also compare favourably with those obtained from stability analysis, 13.44 and 6.64, respectively.

In summary, a major modification of the dynamics in differentially heated cavities

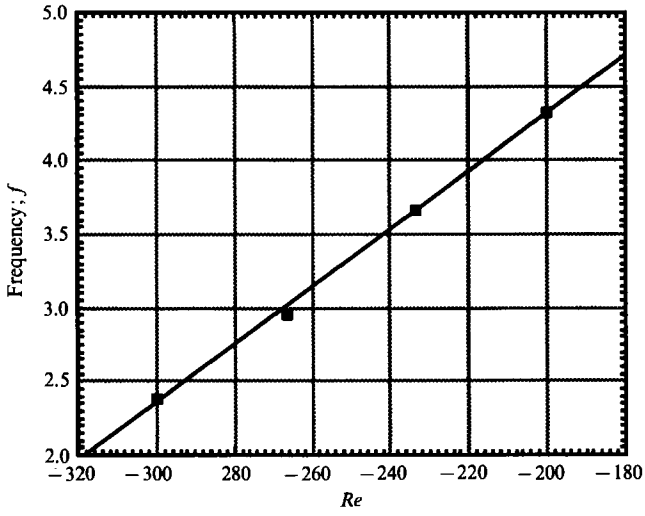

FIGURE 21. Non-dimensional frequency of the simply periodic regimes as a function of Reynolds number for $Gr = 6 \times 10^3$ and two aspect ratios: $A = 12.5$ and 25.

has been shown to occur in a certain range of negative Re. For small $|Re|$, thermocapillarity favoured the onset of an unsteady flow which remains essentially driven by buoyancy forces. In particular, we have not seen the onset of instabilities for the lowest investigated Grashof number, i.e. $Gr = 3 \times 10^3$. This observation is consistent with the results of a stability analysis by Laure & Roux (1989) leading to a lower limiting value of $Gr \approx 5.16 \times 10^3$ (for $Re \approx -300$). For large$|Re|$, oscillations induced by the buoyancy effect can be damped leading to a reverse transition to steady state as for large positive Re. This feature is consistent with the fact that, for a given Gr, the flow structure has to become more and more symmetrical for larger and larger $|Re|$.

6. Steady flow results (large $|Re|$)

6.1. *Effect of aspect ratio; additive case* ($Re > 0$)

As previously mentioned, steady-state solutions prevail in a certain Re-range (which depends on the value of Gr). For the largest aspect ratios, $A = 12.5$ and 25, the multicellular character of the flow becomes more and more pronounced as Re is increased, as can be seen by comparing the streamline patterns for several Reynolds numbers, $Re = 1.33 \times 10^3$, 3.33×10^3 and 10^4 in figures 22, 23 and 24 respectively. The effect of the aspect ratio is also displayed in these figures where the qualitative changes in the structure of the steady flow are clearly visible. In general, a vortex has already appeared near the cold wall for $Re = 0$ and its strength increases with Re; for $A = 12.5$ and 25 additional co-rotating cells are created as the Reynolds number is increased. Most of the flow circulates in a fictitious cavity of much smaller aspect ratio than the actual cavity. Note that for the two Grashof numbers investigated, $Gr = 3 \times 10^3$ and 6×10^3, the flows appear to have a qualitatively similar structure; a multicellular region develops in front of the cold wall and a boundary layer whose thickness decreases with Re forms close to the upper surface. The two regions are more evident at higher Re and in the cellular region numerous corotating cells exist. In the additive case at a given Reynolds number, the number of cells is larger for

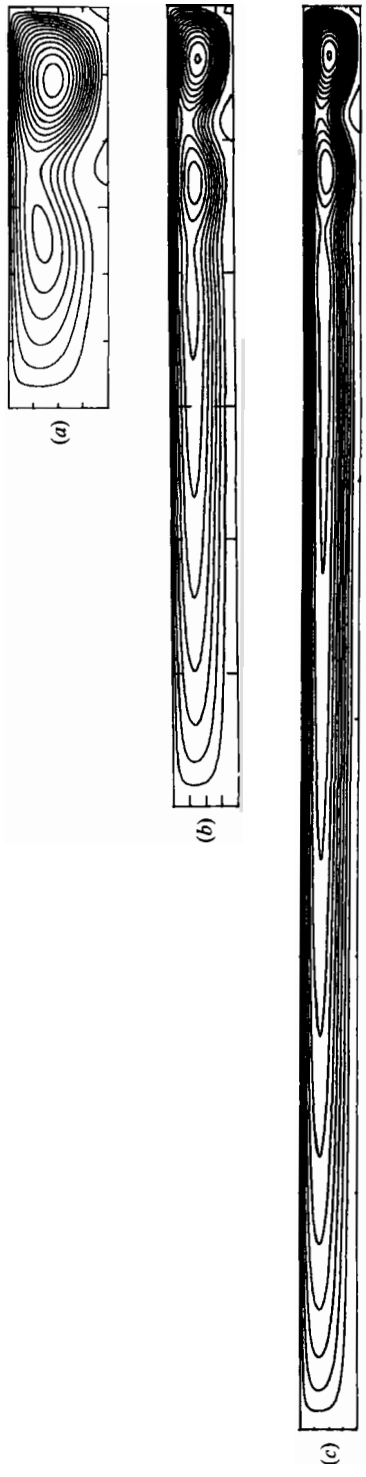

FIGURE 22. Steady flow structures in the additive case for $Gr = 6 \times 10^3$ and $Re = 1.333 \times 10^3$. Streamline patterns for: (*a*) $A = 4$, (*b*) $A = 12.5$ and (*c*) $A = 25$.

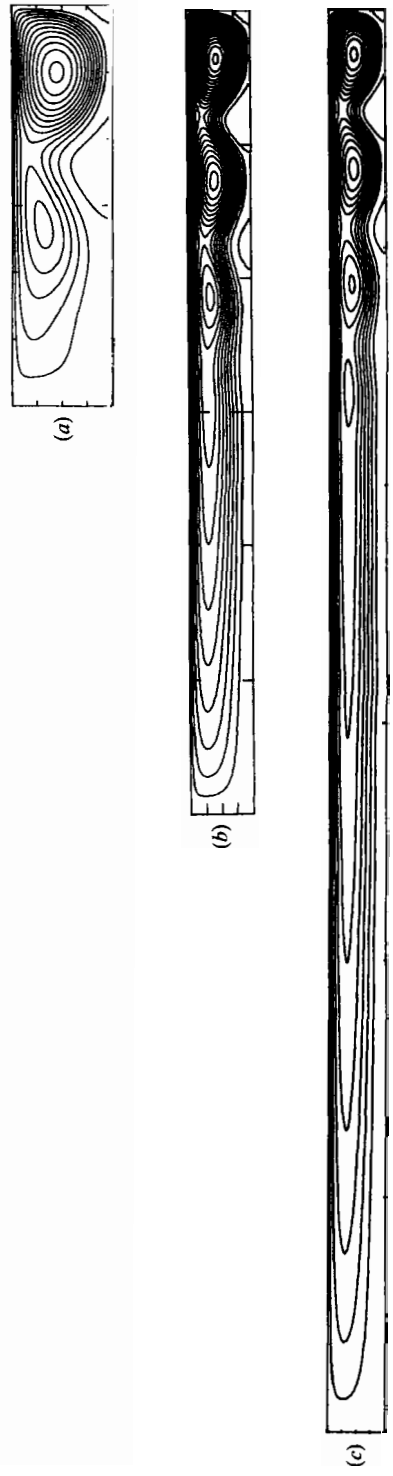

FIGURE 23. As figure 22 but for $Re = 3.333 \times 10^3$.

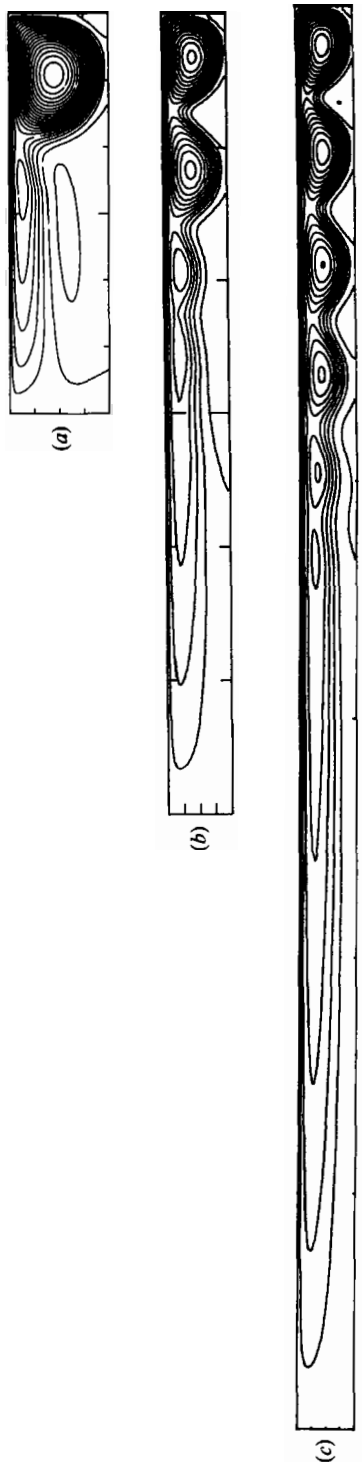

FIGURE 24. As figure 22 but for $Re = 10^4$.

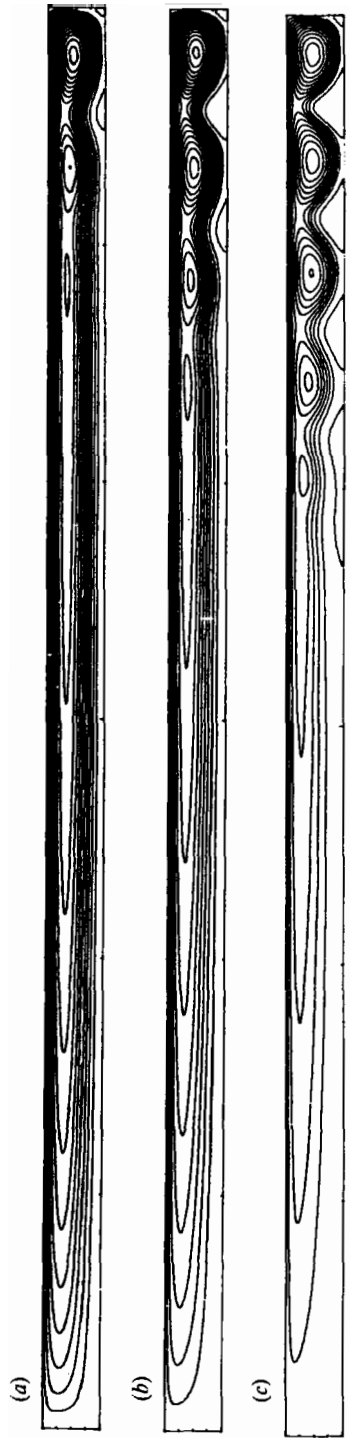

FIGURE 25. Steady flow structures in the additive case for $A = 25$ and $Gr = 3 \times 10^3$. Streamline pattern for: (*a*) $Re = 1.333 \times 10^3$, (*b*) $Re = 3.333 \times 10^3$ and (*c*) $Re = 10^4$.

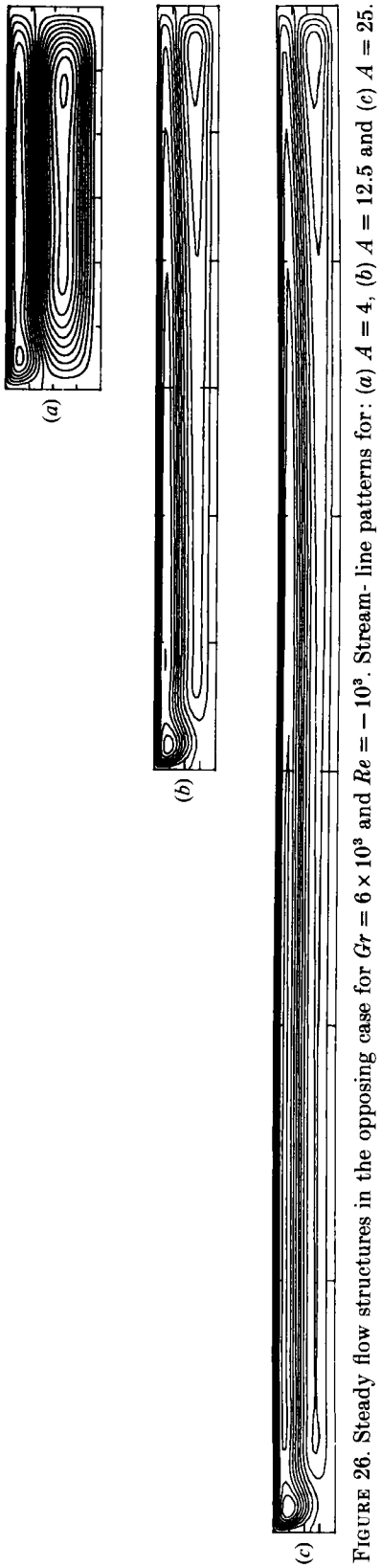

FIGURE 26. Steady flow structures in the opposing case for $Gr = 6 \times 10^3$ and $Re = -10^3$. Stream- line patterns for: (*a*) $A = 4$, (*b*) $A = 12.5$ and (*c*) $A = 25$.

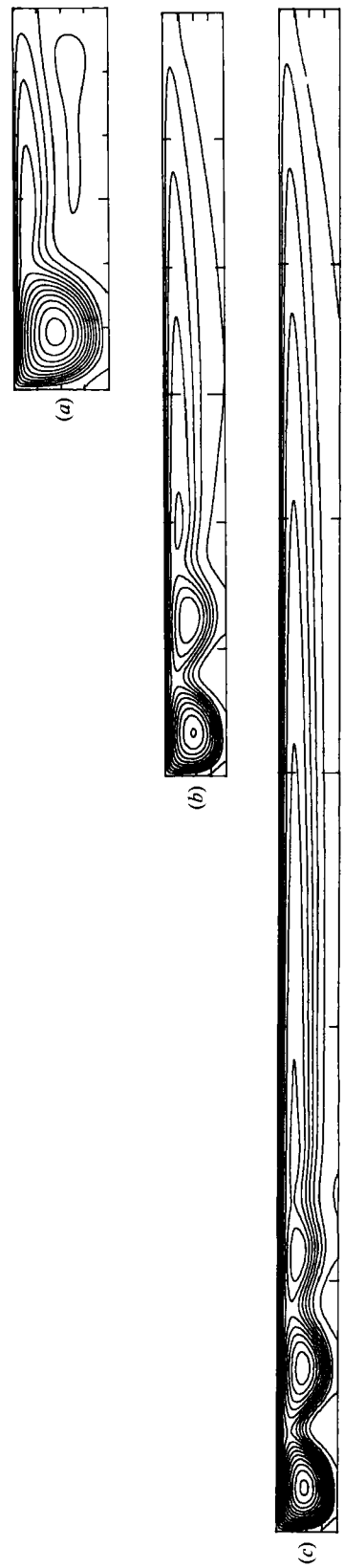

FIGURE 27. As figure 26 but for $Re = -5 \times 10^3$.

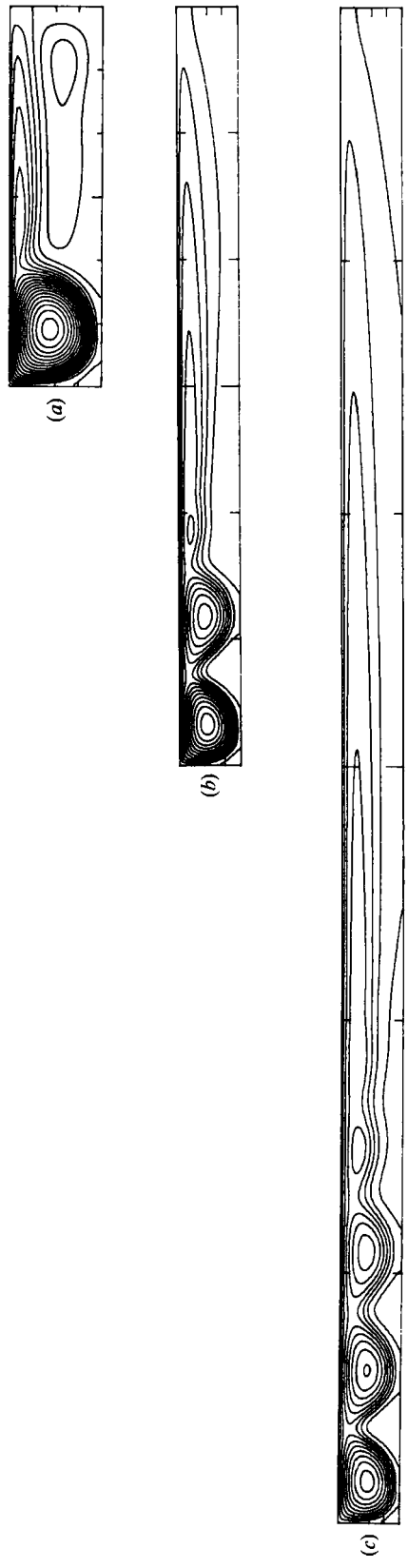

FIGURE 28. As figure 26 but for $Re = -10^4$.

$Gr = 6 \times 10^3$ than for $Gr = 3 \times 10^3$ (see figure 25). Moreover, as Re is further increased counter-rotating flows merge at the bottom wall; the outer one is shown to expand towards the hot isothermal wall and occupy most of the bottom region. Also, the streamlines are more crowded near the free surface, indicating high velocities.

6.2. *Effect of aspect ratio on the flow structure; opposing case* ($Re < 0$)

To focus attention on the case of opposing thermocapillary and buoyancy forces, computations were carried out for $Gr = 3 \times 10^3$ and 6×10^3 and for $|Re| \leqslant 1.67 \times 10^4$ leading to Bd ranging from $-\infty$ to -0.18. The main feature of the flow is that in the range of negative Reynolds numbers investigated, two separated flows occupying the total length of the cavity are shown to exist (figure 26; for $Bd \approx -6$): one is generated by buoyancy forces, rising along the hot wall (left side) and circulating from cold to hot along the bottom wall, while the second is thermocapillary driven, circulating from cold to hot along the upper surface. This behaviour compares well with the numerical results of Villers & Platten (1985) showing two contrarotative cells, and with the experimental results of Villers & Platten (1987*b*) in a rectangular cavity filled with a water-n-heptanol mixture where it was shown that two kinds of convections exist over a certain range of the cavity height. Two separated, counter-rotating cells occupy the cavity, with the upper one thermocapillary driven and the lower one buoyancy driven. Below a certain value of the cavity height the buoyancy-driven cell vanishes. The results presented in figures 27 and 28 for large enough $|Re|$ where thermocapillarity dominates (i.e. $Bd > -6$) can be compared to the case of positive Re; the latter leads to a flow circulating in the opposite direction (from cold to hot along the upper surface) but the main flow structure is qualitatively the same (except for a very small recirculating buoyancy-driven flow in the right bottom corner). Also the emergence of supplementary cells with increasing $|Re|$ can be observed.

It is interesting to note that the calculations of Bergman & Keller (1988) made for smaller aspect ratios, $A = 0.5$, 1 and 2, showed similar flow patterns for a purely buoyancy-driven flow and for the 'additive case'. The latter leads to an increase in the strength of the flow which is evident from the magnitude of the stream function in the centre of the cells. In the opposing case two cells separated by a tilted interface develop in a square cavity ($A = 1$) while in the additive case the patterns are simply one large cell occupying the entire volume. For a large $|Bd|$ (e.g. $Bd\,A^2 = -100$) the flow pattern changes; thermocapillary flow manifests itself in a thin layer close to the upper surface while the buoyant flow dominates over the rest of the cavity.

6.3. *Surface velocity*

The dependence of surface velocity at $y = \frac{1}{2}A$, in terms of Re (for positive and for negative Re) has been analysed for different Gr, in terms of $v^*_{\mathrm{surf}} = v_{\mathrm{surf}} H/\nu$, where v_{surf} is the dimensional surface velocity. The v^*_{surf} curves are displayed in figures 29(*a*) and 29(*b*) for $A = 4$ and $A = 25$ respectively. At sufficiently large $|Re|$, in fact for $Re \approx Gr$, they asymptotically approach the curve for $Gr = 0$ (pure thermocapillary flow), indicating that buoyancy effects become negligible. This is in agreement with the concluding remarks of Metzger & Schwabe (1988) and with the recent results of Bradley & Homsy (1989) who presented scaling analysis and computations for combined convection in a square cavity, showing a dominant thermocapillary effect at large enough Re.

Furthermore, experimental results of Metzger & Schwabe (1988) concerning the surface velocity for different aspect ratios (see their figure 25), and therefore for

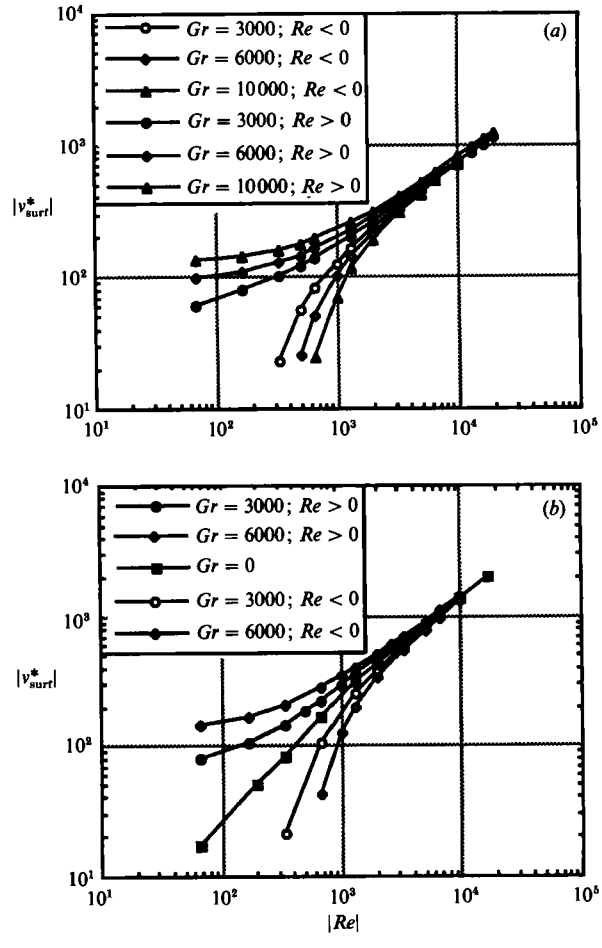

FIGURE 29. Non-dimensional horizontal surface velocity v^*_{surf} as a function of $|Re|$ for various Grashof numbers: (*a*) $A = 4$ and (*b*) $A = 25$.

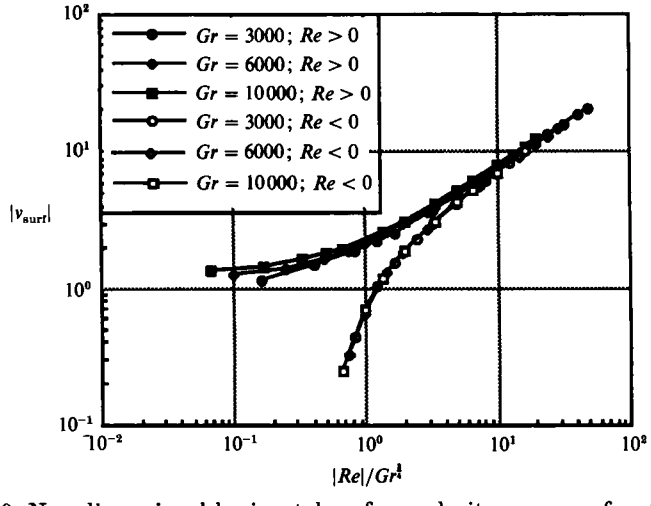

FIGURE 30. Non-dimensional horizontal surface velocity v_{surf} as a function of $|Re|/Gr^{\frac{3}{4}}$ for various Grashof numbers, for $A = 4$.

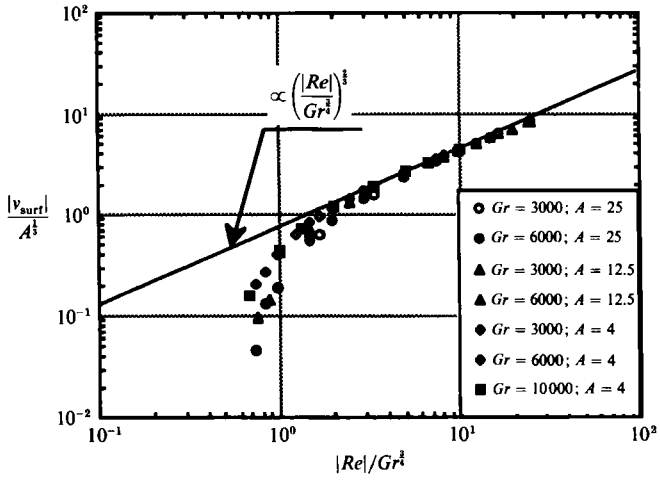

FIGURE 31. Non-dimensional horizontal surface velocity $v_{surf}/A^{\frac{1}{3}}$ as a function of $|Re|/Gr^{\frac{3}{4}}$ for various Grashof numbers and aspect ratio, at $y = \frac{1}{2}A$.

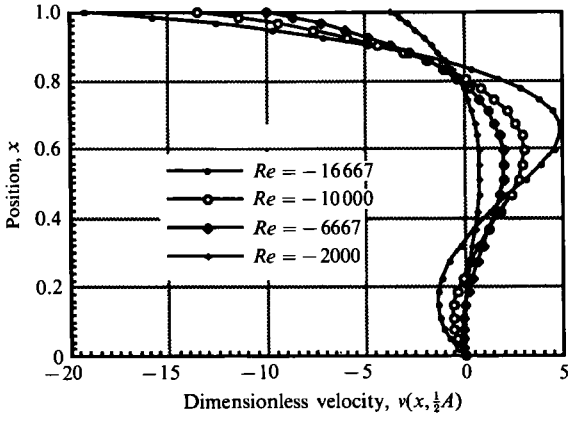

FIGURE 32. Vertical velocity profiles in the opposing case at $y = \frac{1}{2}A$ for $A = 12.5$ and $Gr = 6 \times 10^3$.

different Bond numbers, show that the influence of the increasing Bond number ($1 \leqslant Bd \leqslant 165$) is more effective for deep cavities ($A < 1$) than for shallow cavities ($A > 1$). For $A = 2$ the dominant effect appears to be the thermocapillary flow.

In a previous paper by Ben Hadid *et al.* (1989) the numerical solutions of the dimensionless surface velocity were shown to merge into a single curve when scaled in the following way:

$$v_{surf} = a + b\frac{|Re|^{\frac{2}{3}}}{Gr^{\frac{1}{2}}} \quad \text{or} \quad v_{surf} = \nu/H[aGr^{\frac{1}{2}} + b|Re|^{\frac{2}{3}}], \tag{7}$$

with $a = 2.22$ and $b = -3.15$ for $A = 25$. This correlation is also valid for other aspect ratios like $A = 4$ and 12.5, but with different values of a and b. Figure 30 shows such a correlation, for $A = 4$; it can be compared to figure 29 (a).

A more universal correlation, involving the aspect-ratio effect, can be obtained through the logarithmic plot of $v_{surf}/A^{\frac{1}{3}}$ versus $|Re|/Gr^{\frac{3}{4}}$ as shown in figure 31 for $A = 4$, 12.5 and 25. In this figure the two sets of points for $A = 12.5$ and $A = 25$ fall

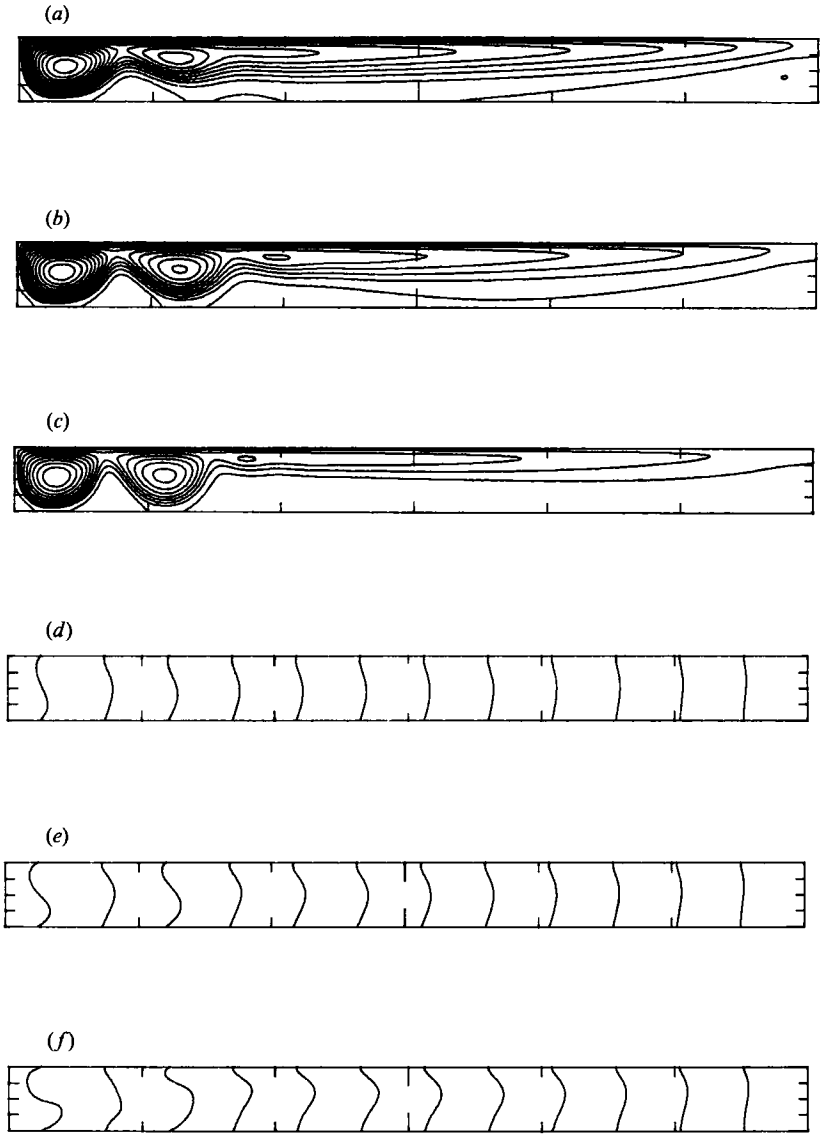

FIGURE 33. Steady flow structures in the opposing case for $A = 12.5$, $Gr = 6 \times 10^3$ and conducting horizontal boundaries. (*a–c*) Streamline patterns for: $Re = -3.333 \times 10^3$, $Re = -6.666 \times 10^3$ and $Re = -1.6667 \times 10^4$, respectively. (*d–f*) Isotherms for $Re = -3.333 \times 10^3$, $Re = -6.666 \times 10^3$ and $Re = -1.6667 \times 10^4$, respectively

onto a single curve. This curve and the curve corresponding to $A = 4$ become closer and closer for increasing $|Re|/Gr^{\frac{3}{4}}$; their slope asymptotically approaching 2.3 (solid line) beyond a particular value of $|Re|/Gr^{\frac{3}{4}}$, close to 3, where the (surface) boundary-layer regime is dominantly induced by thermocapillarity. Such a transition was found previously by Ben Hadid *et al.* (1988) for purely thermocapillary-driven flow. Finally, the following relation is proposed for the boundary-layer regime:

$$|v^*_{\text{surf}}| = A^{\frac{1}{3}}[a'Gr^{\frac{1}{2}} + b'|Re|^{\frac{2}{3}}] \tag{8}$$

where $|v^*_{\text{surf}}| = Gr^{\frac{1}{2}}|v_{\text{surf}}| = \mathrm{H}/\nu|V_{\text{surf}}|$. The values of the constants obtained in this

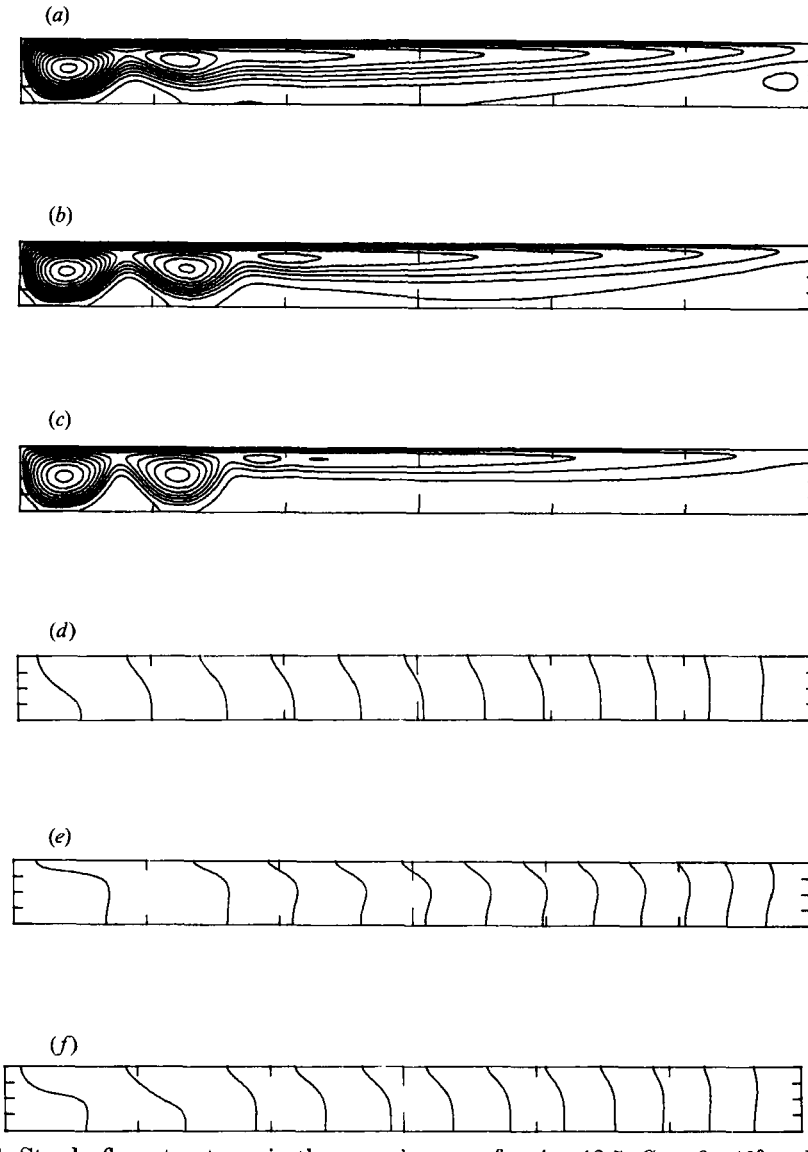

FIGURE 34. Steady flow structures in the opposing case for $A = 12.5$, $Gr = 6 \times 10^3$ and insulated horizontal boundaries. (*a–c*) Streamline patterns for $Re = -3.333 \times 10^3$, $Re = -6.666 \times 10^3$ and $Re = -1.6667 \times 10^4$, respectively. (*d–f*) Isotherms for $Re = -3.333 \times 10^3$, $Re = -6.666 \times 10^3$ and $Re = -1.6667 \times 10^4$, respectively.

study over the range $4 \leqslant A \leqslant 25$, $Gr \leqslant 10^4$ and $|Re| \leqslant 1.7 \times 10^4$ are $a' = 0.75$ and $b' = -1.08$.

A typical dimensionless horizontal velocity profile in the median plane (at $y = \frac{1}{2}A$) with respect to the depth of the cavity is shown in figure 32 for $Gr = 6 \times 10^3$ and various negative Re-values. The role of the thermocapillary flow is more evident from these profiles which change substantially when $|Re|$ increases. The surface velocity continuously increases with $|Re|$, but the variation of the velocity in the lower part of the cavity is no longer monotonic: for small values of $|Re|$ there is a relatively quiescent zone there. When $|Re|$ is further increased, the velocity in the lower part of

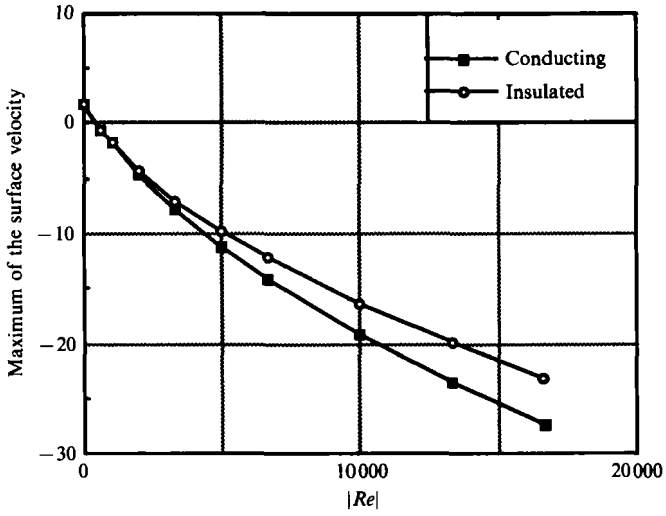

FIGURE 35. Maximum surface velocity v_{surf} as a function of $|Re|$ for $A = 12.5$, $Gr = 6 \times 10^3$.

the cavity increases. This is probably due to the increase of the magnitude of the counter-rotating flow induced by viscous interaction between the surface cell and the cell near the bottom wall. This viscous effect increases as the thermocapillary convection increases. In addition it is noteworthy that the surface cell is more and more concentrated near the free surface when $|Re|$ increases, and thus buoyancy forces become dominant over an increasing portion of the cavity and in particular near the bottom wall.

6.4. *Effects of the thermal boundary conditions; opposing case* ($Re < 0$)

The effect of thermal conditions along the horizontal boundaries on the flow structure and the corresponding thermal field is also interesting. The two limit cases with perfectly conducting and perfectly insulating boundaries have been considered for $A = 12.5$ and $Gr = 6 \times 10^3$ for different negative Reynolds numbers. The streamlines and the thermal fields are displayed in figure 33 for the conducting case, and in figure 34 for the insulating case. For $Re = -3.33 \times 10^3$ (figures 33*d* and 34*d*) the flow exerts only a small effect on the thermal field and for increasing $|Re|$ the influence of the flow on the thermal field increases. Furthermore, at larger values of $|Re|$ ($Re = -6.67 \times 10^3$ and -1.67×10^4) the resulting thermal fields are different, mainly in the cellular regions, while no significant variation in the flow patterns is observed qualitatively. On the right side of the cavity, e.g. the non-cellular flow region, the isotherms are only slightly distorted indicating that the heat transfer is mainly by conduction, while a strong thermal stratification is exhibited on the left side owing to the strong convective motion in the vortex regions., Figure 35 shows the evolution of the maximum surface velocity with respect to $|Re|$, for both the conducting and insulating cases. The two velocity curves merge for low $|Re|$ and separate for $Re \leqslant -2.5 \times 10^3$; a difference of about 16% exists at $Re = -1.67 \times 10^4$, the surface velocity being higher for the conducting case. Finally, the surface temperature evolution is given for the insulating case in figure 36 for $0 \leqslant y \leqslant 5$. (It is imposed and linear in the conducting case.) The surface temperature decreases quite linearly in the right-hand-side region when y increases, but a pronounced curvature exists in the left-hand side (near the hot wall). The temperature deviation

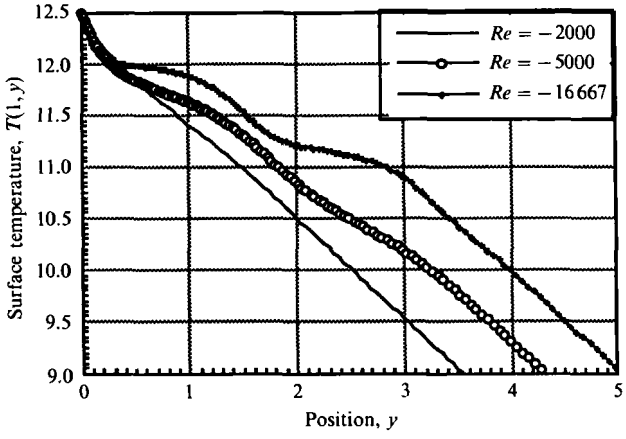

FIGURE 36. Surface temperature profiles for $A = 12.5$, $Gr = 6 \times 10^3$ and several negative Reynolds numbers.

from the linear profile becomes more and more pronounced as $|Re|$ increases, which is consistent with the stronger and stronger circulation observed in figures 27 and 28.

7. Summary and concluding remarks

This study is focused on the convective flow driven by combined buoyancy and thermocapillary forces in shallow cavities for $A \geqslant 4$ and in particular on how the flow regime is related to the relative strength and sense of the two forces. A number of numerical experiments were performed illustrating the influence of the dimensionless governing parameters, Gr, Re and A, on the flow-field variables and the flow regimes. It is demonstrated by numerical simulations that a variety of flow structures and dynamical behaviour can occur in a two-dimensional, combined buoyancy and thermocapillary driven convection when the aspect ratio is equal to 4, 12.5 and 25. The effect of thermocapillary forces on an established buoyant flow has been emphasized for both the additive ($Re > 0$) and opposing ($Re < 0$) cases. For $Re > 0$, a solution was found to converge to a steady-state regime for all the investigated Re-range when started from an established steady buoyancy-driven flow. As Re is increased, several cells successively appear in the cold region where the highest velocity is located. At a given aspect ratio, the maximum number of cells depends on Gr and Re. In the range of Gr-values investigated the influence of the buoyancy force is limited at low Reynolds values. For large Re the thermocapillary flow is nearly independent of Gr and, therefore, is always the dominating factor; there is no appreciable variation in the surface velocity with Grashof number for $Re > 3 \times 10^3$.

For negative Reynolds numbers, however small, the most important result is that an unsteady flow regime can occur, in certain circumstances, even for a value of Grashof number below that obtained in very shallow cavity ($A \to \infty$) for purely buoyancy-driven convection, e.g. $Gr = 6 \times 10^3$. The flow which would be steady in the buoyancy-driven case, changes from steady to unsteady multicellular flow and returns to steady multicellular flow upon increasing $|Re|$. It is not obvious why the possibility of an oscillatory state is enhanced but it undoubtedly is of dynamical nature; the combined flow seems to be least stable in a specific range $-0.08 < Re/Gr < -0.013$. The likelihood of the onset of an oscillatory regime for

a subcritical Grashof number probably can be correlated with some property of the velocity profile (e.g. the displacement of the inflexion point of the velocity). For example, in the Tollmien–Schlichting boundary-layer stability results, for forced convection, the role of such an inflexion point in the velocity profile has been proven. From the analytical expression of the horizontal velocity (assuming the flow to be steady for an infinite long layer $A \to \infty$ and $u = 0$, $v = v(x)$; see e.g. Kirdyashkin 1984) such an inflexion point has to occur in the interval $0 \leqslant x \leqslant 1$, in the range $-0.416 \leqslant Re/Gr \leqslant 0.25$.

We also note that for small Grashof number (e.g. $Gr = 3 \times 10^3$), a steady-state solution prevails in the whole range of Reynolds numbers investigated. We suspect that there is a critical Grashof number below which the effect of the thermocapillary forces is no longer destabilizing. This conclusion is supported by a linear stability analysis which leads to a limiting Grashof number equal to 5.156×10^3. We have not precisely determined the critical destabilizing (stabilizing) Reynolds number for which the resulting combined flow attains a new unsteady (steady) state. To locate such a critical value requires a very detailed search and even in two-dimensional simulations this requires a prohibitively long computing time.

Unfortunately, there appear to be no data available in the literature for comparison. More experimental work as well as modelling must be done in order to glean more insight into the various flow regimes (velocity fields and flow structures).

We are grateful for comments from Professor Robert Sani (University of Colorado-Boulder, USA). The authors also wish to thank J. J. Favier, D. Camel and P. Tison (L.E.S. of C.E.N.G.) for enlightening discussions. This work was supported by the Centre National d'Etudes Spatiales (Division Microgravité Fondamentale et Appliquée). Computations were carried out on the Cray-2 computer, with support from the Centre de Calcul Vectoriel pour la Recherche (CCVR). The authors also wish to acknowledge the Centre National Universitaire Sud de Calcul (CNUSC) and the Point d'Accès St. Charles.

REFERENCES

Azouni, M. A. 1981 Time-dependent natural convection in crystal growth systems. *PhysicoChem. Hydrodyn.* **2**, 295–309.

Ben Hadid, H. 1989 Etude numérique des mouvements convectifs au sein des fluides de faible nombre de Prandtl. Thèse de Doctorat d'Etat, University of Aix-Marseille II, France.

Ben Hadid, H., Laure, P. & Roux, B. 1989 Thermocapillarity effect on the stability of buoyancy-driven flows in shallow cavities. *PhysicoChem. Hydrodyn.* **11**, 625–644.

Ben Hadid, H. & Roux, B. 1989 Buoyancy- and thermocapillary-driven flow in a shallow open cavity: unsteady flow regimes. *J. Cryst. Growth* **97**, 217–225.

Ben Hadid, H. & Roux, B. 1990*a* Buoyancy-driven oscillatory flows in shallow cavities filled with low-Prandtl-number flows. In *Numerical Simulation of Oscillatory Convection in Low-Pr Fluids* (ed. B. Roux), pp. 25–34. Vieweg.

Ben Hadid, H. & Roux, B. 1990*b* Thermocapillary convection in long horizontal layers of low-Prandtl-number melts subject to horizontal temperature gradient. *J. Fluid Mech.* **221**, 77–103.

Ben Hadid, H., Roux, B., Laure, P., Tison, P., Camel, D. & Favier, J. J. 1988 Surface tension-driven flows in horizontal liquid metal layers. *Adv. Space Res.* **8**, 293–304.

Bergman, T. L. & Keller, J. R. 1988 Combined buoyancy surface-tension flow in liquid metals. *Numer. Heat Transfer* **13**, 49–63.

Bergman, T. L. & Ramadhyani, S. 1986 Combined buoyancy- and thermocapillary-driven convection in open square cavities. *Numer. Heat Transfer* **9**, 441–451.

BIRIKH, R. V. 1966 Thermocapillary convection in horizontal layer of liquid. *J. Appl. Mech. Tech. Phys.* **7**, 43–49.

BRADLEY, M. C. & HOMSY, G. M. 1989 combined buoyancy-thermocapillary flow in a cavity. *J. Fluid Mech.* **207**, 121–132.

CAMEL, D. & FAVIER, J. J. 1988 Transport processes during directional solidification and crystal growth: scaling and experimental study. In *Physico-Chemical-Hydrodynamics Interfacial Phenomena* (ed. M. G. Velarde), NATO ASI Series, B: vol. 174, pp. 595–618.

CAMEL, D., TISON, P & FAVIER, J. J. 1985 Marangoni flow regimes in liquid metals. *Acta Astronautica* **13**, 723–726.

CARRUTHERS, J. R. 1977*a* Crystal growth in low gravity environment. *J. Cryst. Growth* **42**, 379–385.

CARRUTHERS, J. R 1977*b* Thermal convection instabilities relevant to crystal growth from liquids. In *Preparation and Properties of Solid State Materials*, Vol. 3 (ed. W. R. Wilcox & R. A. Lefever). Marcel Dekker.

CHUN, CH. H 1980 Experiments on steady and oscillatory temperature distribution in a floating zone due to the Marangoni convection. *Acta Astronautica* **7**, 479–488.

CUVELIER, C. & DRIESSEN, J. M. 1986 Thermocapillary free boundaries in crystal growth. *J. Fluid Mech.* **169**, 1–26.

DAVIS, S. H. 1987 Thermocapillary instabilities. *Ann. Rev. Fluid Mech.* **19**, 403–435.

FAVIER, J. J., ROUZAUD, A. & COMERA J. 1986 Influence of various hydrodynamic regimes in melts on solidification interface. *Rev. Phys. Appl.* **22**, 195–200.

GERSHUNI, G. Z., ZHUKHOVITSKY, E. M. & NEPOMNIASHCHY, A. A. 1989 *Stability of Convective Flows*. Moscow: Nauka.

HIRSH, R. 1975 Higher order accurate difference solutions of fluid mechanics problems by a compact differencing technique. *J. Comput. Phys.* **19**, 90–109.

HURLE, D. T. J. 1967 Thermo-hydrodynamic oscillation in liquid metals: the cause of impurities striations in melt-grown crystals. *J. Phys. Chem. Solids* Suppl. no. 1, 659–669.

HURLE, D. T. J. 1983 Convective transport in melt growth systems. *J. Cryst. Growth* **65**, 124–132.

HURLE, D. T. J., JAKEMAN, E. & JOHNSON, C. P. 1974 Convective temperature oscillations in molten Gallium. *J. Fluid Mech.* **64**, 565–576.

KAMOTANI, Y., OSTRACH, S. & LOWRY, S. 1982 An experimental study of heat induced surface-tension driven flow. In *Materials Processing in the Reduced Gravity Environment of Space* (ed. G. E. Rindone), pp. 161–171. North-Holland.

KIRDYASHKIN, A. G. 1984 Thermogravitational and thermocapillary flows in a horizontal liquid layer under the conditions of a horizontal temperature gradient. *Intl J. Heat Mass Transfer* **27**, 1205–1218.

LAMPRECHT, R., SCHWABE, D. & SCHARMANN, A. 1990 Thermocapillary and buoyancy convection in an open cavity under normal and reduced gravity. *J. Fluid Mech.* (submitted).

LANGLOIS W. E. 1985 Buoyancy-driven flows in crystal-growth melts. *Ann. Rev. Fluid Mech.* **17**, 191–215.

LAURE, P. & ROUX, B. 1987 Synthèse des résultats obtenus par l'étude de stabilité des mouvements de convection dans une cavité horizontale de grande extension. *C.R. Acad. Sci. Paris* II, **305**, 1137–1143.

LAURE, P. & ROUX, B. 1989 Linear and non-linear analyses of the Hadley circulation. *J. Cryst. Growth* **97**, 226–234.

LEVICH, V. G. & KRYLOV, V. S. 1969 Surface tension-driven phenomena. *Ann. Rev. Fluid Mech.* **1**, 293–316.

METZGER, J. & SCHWABE, D. 1988 Coupled buoyant and thermocapillary convection. *PhysicoChem. Hydrodyn.* **10**, 263–282.

MÜLLER, G. 1988 Convection and inhomogeneities in crystal growth from the melt. In *Crystals, Properties, and Applications*, vol. 12. Springer.

MYZNIKOV, V. B. 1981 On the stability of steady advective motion in a horizontal layer with a free boundary relative to space disturbances. In *Convective Flow* (ed. E. M. Zukhovitskii), vol. 76, pp. 76–83. Perm State Pedagogical Institute.

OSTRACH, S. 1982 Low-gravity fluid flows. *Ann. Rev. Fluid Mech.* **14**, 313–345.

OSTRACH, S. & PRADHAN, A. 1978 Surface-tension induced convection at reduced gravity. *AIAA J.* **16**, 419–424.

PIMPUTKAR, S. M. & OSTRACH, S. 1981 Convective effects in crystal grown from melts. *J. Cryst. Growth* **55**, 614–646.

POLEZHAEV, V. I. 1984 *Hydrodynamics of Heat and Mass Transfer During Crystal Growth.* Springer.

PULICANI, J. P. 1989 Application des méthodes spectrales à l'étude d'écoulements de convection. Ph.D. thesis, University of Nice, France.

RANDRIAMAMPIANINA, A., CRISPO DEL ARCO, E., FONTAINE, J. P. & BONTOUX, P. 1990 Spectral method for two-dimensional time-dependent $Pr \rightarrow 0$ convection. In *Numerical Simulation of Oscillatory Convection in Low-Pr Fluids* (ed. B. Roux), pp. 224–255. Vieweg.

ROUX, B. (ed.) 1990 *GAMM Workshop: Numerical Simulation of Oscillatory Convection in Low-Pr Fluids.* Notes on Numerical Fluid Mechanics, vol. 27. Vieweg.

ROUX, B., BEN HADID, H. & LAURE, P. 1989 Hydrodynamical regimes in metallic melts subjects to a horizontal temperature gradient. *Eur. J. Mech.* B **8**, 375–396.

ROUX, B., BONTOUX, P., LOC, T. P. & DAUBE, O. 1979 *Optimisation of Hermitian Methods for N.S. Equations in Vorticity and Stream Function Formulation.* Lecture Notes in Mathematics, vol. 771, pp. 450–468. Springer.

ROSENBERGER, F. 1979 *Fundamentals of Crystal Growth.* Springer.

SCHWABE, D. 1988 Surface-tension-driven flow in crystal growth melts. In *Crystals*, vol. 11, pp. 75–112. Springer.

SCHWABE, D. & SCHARMANN, A. 1981 The magnitude of thermocapillary convection in large melt volumes. *Adv. Space. Res.* **1**, 13–16.

SMITH, M. K. & DAVIS, S. H. 1983 Instabilities of dynamic thermocapillary liquid layers. Part 1. Convective instabilities. *J. Fluid Mech.* **132**, 119–144.

STRANI, M., PIVA, R. & GRAZIANI, G. 1983 Thermocapillary convection in a rectangular cavity: asymptotic theory and numerical simulation. *J. Fluid Mech.* **130**, 347–376.

THOMPSON, J. F., THAMES, F. C. & MASTIN, C. W. 1974 Automatic numerical generation of a body-fitted curvilinear system. *J. Comput. Phys.* **15**, 299–319.

UTECH, H. P., BROWER, S. W. & EARLY, J. G. 1967 Thermal convection and crystal growth in horizontal boats: flow pattern, velocity measurements, and solute distribution. In *Crystal Growth* (ed. Peiser), pp. 201–205. Pergamon.

VILLERS, D. 1989 Couplage entre les convections capillaire et thermogravitationnelle. Ph.D. thesis, University of Mons, Belgium.

VILLERS, D. & PLATTEN, J. K. 1985 Marangoni convection in systems presenting a minimum in surface tension. *PhysicoChem. Hydrodyn.* **6**, 435–451.

VILLERS, D. & PLATTEN, J. K. 1987*a* Separation of Marangoni convection from gravitational convection in earth experiments. *PhysicoChem. Hydrodyn.* **8**, 173–183.

VILLERS, D. & PLATTEN, J. K. 1987*b* Thermocapillary convection when surface tension increases with temperature: comparison between numerical simulations and experimental results by LDV. In *Numerical Methods in Laminar and Turbulent Flow* (ed. C. Taylor), vol. 5, pp. 1268–1279. Pineridge.

VILLERS, D. & PLATTEN, J. K. 1990 Influence of thermocapillarity on the oscillatory convection in low-*Pr* fluids. In *Numerical Simulation of Oscillatory Convection in low-Pr Fluids* (ed. B. Roux), pp. 108–115. Vieweg.

WILKE, H. & LÖSER, W. 1983 Numerical calculation of Marangoni convection in a rectangular open boat. *Crystl Res. Technol.* **6**, 825–833.

WINTERS, K. H. 1988 Oscillatory convection in liquid metals in a horizontal temperature gradient. *Intl J. Numer. Methods Engng* **25**, 401–414.

WINTERS, K. H. 1990 A bifurcation analysis of oscillatory convection in liquid metals. In *Numerical Simulation of Oscillatory Convection in low-Pr Fluids* (ed. B. Roux), pp. 319–326. Vieweg.

WINTERS, K. H., CLIFFE, K. A. & JACKSON, C. P. 1987 The prediction of instabilities using

bifurcation theory. *Harwell Rep.* HL86/1147. (Published in *Transient and Coupled Systems* (ed. R. W. Lewis, E. Hinton, P. Bettes & B. A. Schrefer). Wiley.)

YIH, C. S. 1968 Fluid motion induced by surface-tension variation. *Phys. Fluids* **3**, 477–480.

ZEBIB, A., HOMSY, G. M. & MEIBURG, E. 1985 High Marangoni number convection in a square cavity. *Phys. Fluids* **28**, 3467–3476.